

# Ferroelectric transistors based on shear-transformation-mediated rhombohedral-stacked molybdenum disulfide

Received: 13 February 2023

Accepted: 19 October 2023

Published online: 30 November 2023

 Check for updates

Tilo H. Yang  , Bor-Wei Liang<sup>1,2</sup>, Hsiang-Chi Hu<sup>1</sup>, Fu-Xiang Chen , Sheng-Zhu Ho<sup>4</sup>, Wen-Hao Chang<sup>1</sup>, Liu Yang , Han-Chieh Lo<sup>1</sup>, Tzu-Hao Kuo , Jyun-Hong Chen<sup>2</sup>, Po-Yen Lin<sup>6</sup>, Kristan Bryan Simbulan , Zhao-Feng Luo<sup>8</sup>, Alice Chinghsuan Chang<sup>9</sup>, Yi-Hao Kuo<sup>3</sup>, Yu-Seng Ku<sup>10</sup>, Yi-Cheng Chen , You-Jia Huang<sup>1</sup>, Yu-Chen Chang<sup>1</sup>, Yu-Fan Chiang<sup>1</sup>, Ting-Hua Lu , Min-Hung Lee , Kai-Shin Li<sup>2</sup>, Menghao Wu , Yi-Chun Chen , Chun-Liang Lin , & Yann-Wen Lan  

To develop low-power, non-volatile computing-in-memory device using ferroelectric transistor technologies, ferroelectric channel materials with scaled thicknesses are required. Two-dimensional semiconductors, such as molybdenum disulfide ( $\text{MoS}_2$ ), equipped with sliding ferroelectricity could provide an answer. However, achieving switchable electric polarization in epitaxial  $\text{MoS}_2$  remains challenging due to the absence of mobile domain boundaries. Here we show that polarity-switchable epitaxial rhombohedral-stacked (3R)  $\text{MoS}_2$  can be used as a ferroelectric channel in ferroelectric memory transistors. We show that a shear transformation can spontaneously occur in 3R  $\text{MoS}_2$  epilayers, producing heterostructures with stable ferroelectric domains embedded in a highly dislocated and unstable non-ferroelectric matrix. This diffusionless phase transformation process produces mobile screw dislocations that enable collective polarity control of 3R  $\text{MoS}_2$  via an electric field. Polarization–electric-field measurements reveal a switching field of  $0.036 \text{ V nm}^{-1}$  for shear-transformed 3R  $\text{MoS}_2$ . Our sliding ferroelectric transistors are non-volatile memory units with thicknesses of only two atomic layers and exhibit an average memory window of  $7 \text{ V}$  with an applied voltage of  $10 \text{ V}$ , retention times greater than  $10^4$  seconds and endurance greater than  $10^4$  cycles.

Ferroelectric field-effect transistors (Fe-FETs) are three-terminal circuit elements that can function as non-volatile memory elements and could be of use in the development of in-memory computing applications<sup>1–5</sup>. Fe-FETs offer better endurance and shorter read/write times

than other emerging memories and can provide non-destructive data readout. Dimensional scaling can increase the embedded memory density and read/write speed and reduce the write voltage down to on-chip, logic-compatible levels<sup>6</sup>. From a technology standpoint, the

A full list of affiliations appears at the end of the paper.  e-mail: [thy@mit.edu](mailto:thy@mit.edu); [clin@nycu.edu.tw](mailto:clin@nycu.edu.tw); [ywlan@ntnu.edu.tw](mailto:ywlan@ntnu.edu.tw)

ferroelectric layer must be scaled from the current state-of-the-art of 5–10 nm to less than 3 nm to fit into the tight pitch of advanced technology nodes<sup>1,7</sup>. However, the out-of-plane ferroelectric dipoles of existing ferroelectrics tend to be suppressed at a scale of a few nanometres due to the incomplete screening of the depolarization field<sup>8,9</sup>.

Recent studies with ferroelectric oxides have shown that ferroelectricity can be retained in sub-3-nm HfO<sub>2</sub> and ZrO<sub>2</sub> (refs. 7,10), leading to encouraging device metrics for ultra-scaled non-volatile memory<sup>11,12</sup>. Two-dimensional (2D) van der Waals (vdW) ferroelectrics are also considered promising materials for such applications following the discovery of sliding ferroelectricity in the vdW interface between two marginally stacked boron nitride (BN) monolayers<sup>13,14</sup>. These sliding ferroelectrics are of particular interest because robust atomic-scale ferroelectricity may be of use in a range of applications.

An out-of-plane polarization can originate from the net charge transfer across the vdW interface as the inversion symmetry of the vdW material is broken<sup>13–15</sup>. This property has been experimentally demonstrated in rhombohedral-stacked (3R) transition metal dichalcogenides (TMDs)<sup>16,17</sup> and amphidynamic polymers<sup>18</sup>. However, investigations of sliding ferroelectricity have relied on scanning-probe-based techniques and localized measurements, and the device performance of sliding-ferroelectricity-based Fe-FETs has remained unclear. Although the growth of 2D 3R-TMD crystals has been widely studied, ferroelectric hysteresis in the transfer characteristics of an FET has yet to be demonstrated for 3R-TMD epitaxial films<sup>16,19,20</sup>. This explains why intrinsic ferroelectricity was rarely noticed, even though it universally exists in 3R-vdW crystals.

In ideal 3R bilayers (space group *R3m*), two layers are parallel stacked without lattice misalignment: that is, the twist angle ( $\theta$ ) between them is 0°. Interlayer sliding along the vdW interface allows various combinations of stacking order (crystallographically known as 3R polytypes). Two of them have been shown to hold a net charge transfer at the interface, denoted as the AB- and BA-stacking configurations<sup>16,17</sup>. From a thermodynamics perspective, they are the most stable stacking configurations among 3R polytypes due to their equal ground-state energies (Fig. 1a).

Similar to conventional ferroelectrics, electric polarization switching must be accompanied by a microstructural redistribution of oppositely polarized domains, in which the process is dominated by the movement of domain boundaries. However, domain boundaries are typically absent in epitaxially-grown 3R-TMDs<sup>16,20</sup>, though in some cases such line defects are induced by topological defects on substrates<sup>21</sup>. Strong edge pinning inhibits the formation of domain boundaries even under an electric field larger than the coercive field<sup>16</sup>. The absence of mobile domain boundaries makes occurrence of polarization switching extremely difficult in 3R MoS<sub>2</sub> epilayers, even though a switching barrier of ~7.09 meV per formula unit is required for BA–AB switching.

Here, we show that a spontaneous nonpolar–polar phase transformation (Fig. 1b) can lead to the formation of mobile partial dislocations in epitaxial 3R MoS<sub>2</sub>, enabling reversible ferroelectric switching under an electric field. Based on this mechanism, we fabricate instances of a sliding ferroelectric semiconductor field-effect transistor (FeS-FET) with non-volatile memory behaviour at thicknesses of only two atomic layers. Our devices have an average memory window of 7 V with an applied voltage of 10 V, retention greater than 10<sup>4</sup> seconds and endurance greater than 10<sup>4</sup> cycles.

## Mixed domains structure in 3R MoS<sub>2</sub> epitaxial film

Chemical vapour deposition (CVD) is used to synthesize 3R MoS<sub>2</sub> films with the desired microstructure (that is, mobile domain boundaries) on SiO<sub>2</sub>/Si substrates (Methods and Extended Data Fig. 1). Material characterizations are performed using transmission electron microscopy (TEM) (Fig. 1d–g) and spectroscopic analyses (Supplementary Figs. 1, 2). Our 3R MoS<sub>2</sub> forms bilayer nanoribbons distributed in parallel (Fig. 1c), which is attributed to the lattice symmetry-directed growth

operated in the diffusion-limited aggregation regime<sup>22,23</sup> (Methods, Extended Data Fig. 2 and Supplementary Note 1). The bilayer nanoribbon possesses a heterogenous lamella triple-phase microstructure where lamellar AB and BA domains are embedded in an AA matrix (Fig. 1d,e). The AA phase is rarely observed in ordinary 3R MoS<sub>2</sub> synthesis due to its energetic instability (Fig. 1a). We obtained an AA-dominant matrix by low-temperature tempering in a molybdenum-deficient condition. Statistical analyses reveal that the yields of potential 3R MoS<sub>2</sub> flakes are highly tunable and reach about 90% in an optimized condition (Supplementary Fig. 3), indicating stable and reproducible growth results via the proposed CVD recipe. The tempered AA nanoribbon possesses heterogeneous domain boundaries and subdomain structures. Most AB and BA lamellae form at the concave corner of the AA matrix (Fig. 1d and Extended Data Fig. 3a,b), while some appear in pairs in the AA matrix (Fig. 1e). These stable lamellae are Shockley-type stacking faults in the AA matrix (Extended Data Fig. 3c). The domain boundaries are 1–2 nm wide and constitute partial screw dislocations with Burgers vector **b** parallel to the  $\langle 0\bar{1}\bar{1}0 \rangle$  (zigzag) direction (Fig. 1f and Extended Data Fig. 3d–g for detailed dislocation analysis). The 3R MoS<sub>2</sub> we produced differs from the ordinary epitaxial 3R MoS<sub>2</sub>, where the formation of domain boundaries is suppressed. Since the initial structure constitutes unstable AA stacking (referring to a non-ferroelectric stacking configuration), it spontaneously decomposes into ferroelectric AB or BA domains, which is driven by the lowering of the total stacking energy (Fig. 1a). Consequently, the possibility of forming domain boundaries is largely increased for our 3R MoS<sub>2</sub>. Spectroscopic analysis shows strain signatures, revealing the large-scale simultaneous phase transition in the entire bilayer flake (Supplementary Fig. 1). Notably, the shear transformation on epitaxial 3R MoS<sub>2</sub> can induce similar dislocation type and Burgers vector as that observed in marginally twisted 3R-TMD bilayers<sup>24</sup>, even though such an interlayer twist is observed only near the domain boundaries as the separated domains remain free of lattice misalignment (Fig. 1f and Extended Data Fig. 4). Following a similar sliding mechanism, the constituent Shockley partials can serve as mobile domain boundaries, as recently reported in the Kelvin-probe force microscopy study<sup>16</sup>. Some thin bilayer nanoribbons that are observed possess only alternating AB and BA domains at the full expense of the early-formed AA domain (Fig. 1g). This strongly indicates that the domain evolutions are associated with the propagation of domain boundaries.

## Verification of ferroelectricity in 3R MoS<sub>2</sub>

To investigate the ferroelectric behaviour of shear-transformed (ST) 3R MoS<sub>2</sub> flakes, piezoelectric force microscopy (PFM) measurements were performed in the off-field mode (Methods). Off-field piezoresponse hysteresis loops were used to examine the ferroelectric properties, specifically to eliminate the electrostatic contribution. In Fig. 2a, the observed butterfly and hysteresis loops of PFM amplitude and phase versus constant-voltage bias indicate characteristic polarization switching found in ferroelectric materials. The presence of ferroelectricity in our ST-3R MoS<sub>2</sub> flakes and the ability of local point switching upon biased tip contact are confirmed by the PFM hysteresis loops. However, it is important to note that domain boundaries would dominate the collective polar control of entire 3R MoS<sub>2</sub> films.

To visualize the electro-mechanical responses of ST-induced dislocations to an electric field perpendicular to the interface, as well as the associated domain evolutions in ST-3R MoS<sub>2</sub> flakes, PFM phase and signal images were acquired before and after poling, as shown in Fig. 2b,c. Before poling, a heterogeneous structure of oppositely polarized lamellar domains resembling those observed in STEM images was observed. Within the poling area, domain flipping occurred during oppositely biased scans, for which detailed phase analysis is shown in Supplementary Fig. 4. Significantly, adjacent areas to the poling region also exhibited a redistribution of domain boundaries in response to the applied electric fields. When scanning with –3.4 V sample bias

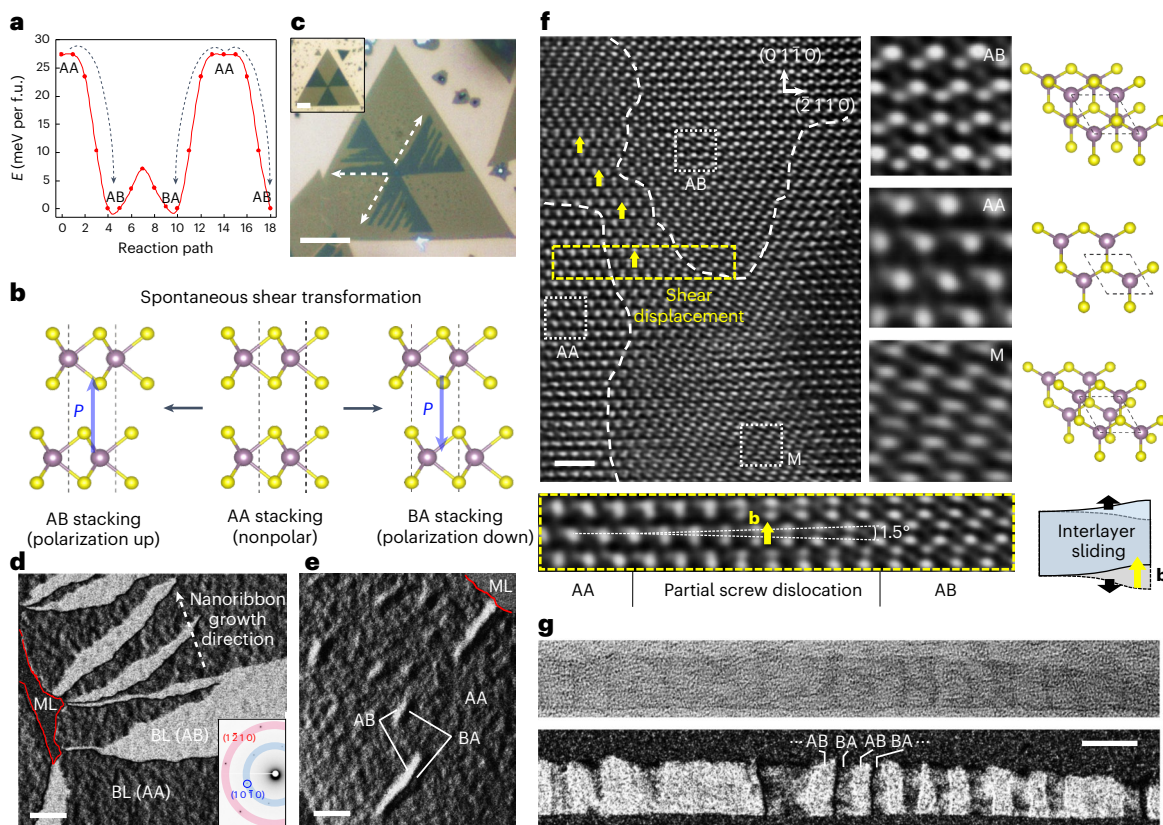


**Fig. 1 | Epitaxial 3R bilayer MoS<sub>2</sub> with switchable electric polarization.** **a**, Ferroelectric switching pathway along an armchair direction of 3R-stacked bilayer MoS<sub>2</sub>. The highest-energy states correspond to the AA-stacking configurations, while the AB and BA stackings possess equal minimum stacking energies. The calculated switching barrier between the AB and BA stacking is 7.09 meV per formula unit, abbreviated f.u. in the figure. **b**, The spontaneous evolution from the unstable AA-stacking phase to the stable AB- or BA-stacking phase. The interfacial polarized phenomenon presents in the AB (upward polarization) and BA (downward polarization) stackings. The S (Mo) atoms from the upper layer lie on top of the Mo (S) atoms from the lower layer in AB (BA) stacking. In the nonpolar AA phase, the net charge transfer between different layers is null, corresponding to its stacking structure, in which the same atoms from the upper and lower layers completely overlap along the z-axis. **c**, Optical micrograph of CVD-grown 3R MoS<sub>2</sub> homoepitaxial patterns on a SiO<sub>2</sub>/Si substrate. Inset: optical micrograph of a fully grown 3R MoS<sub>2</sub> homoepitaxial film.

Scale bars, 10 μm. **d,e**, Tilted dark-field TEM images obtained by filtering the (10̄10) diffraction spot of MoS<sub>2</sub> (denoted in the inset to **d**), demonstrating lamellar AB and BA domains nucleate from the edge (**d**) or inside an AA matrix that occupies most of the bilayer nanoribbon (**e**). The red line (**d** and **e**) marks the edge of the bilayer nanoribbons. ML, monolayer; BL, bilayer. The white dashed arrow points to the growth direction of the bilayer nanoribbon. Scale bars, 100 nm. **f**, Scanning TEM-annular dark-field (STEM-ADF) image demonstrating a representative AB-AA domain boundary, consisting of a 2-nm-wide partial screw dislocation with Burgers vector **b** || (01̄10). Selected regions are shown magnified with the corresponding atomic illustration. Scale bar, 1 nm. **M**, moiré-like transition zone. **g**, Top, tilted bright-field and bottom, dark-field TEM images showing a thin bilayer nanoribbon consisting of alternating AB and BA domains. Scale bar, 25 nm (for the SADP and STEM-ADF results, see Extended Data Fig. 5).

(first poling, depicted by yellow square), subsequent PFM images show that the blue domains (downward polarization) increased while the red domains (upward polarization) decreased. And after a successive scan with +3.6 V (second poling, depicted by black square), the red domains expanded at the expense of the blue domains. Thus, the movement of ST-induced dislocations can be initiated by applying positive or negative electric fields.

## Ferroelectric polarization characteristics in ST-3R MoS<sub>2</sub>

To confirm the switchable electric polarization directly in the ST-3R MoS<sub>2</sub>, we have investigated the polarization states by employing both the scanning probe-based approach (Supplementary Fig. 5 and Note 2) and the polarization–electric-field (*P*–*E*) measurement method (Fig. 2d–g; Methods). Although the former allows us to acquire ferroelectric switching signatures from a nanoscale region, it is irrelevant to the existing domain boundaries because interlayer sliding could occur under a local strong electric field. In contrast, *P*–*E*

characterization provides device-level, collective electric response from an entire device. Since MoS<sub>2</sub> is a semiconductor rather than an insulator, it is challenging to perform standard electrical characterizations of ferroelectricity. To overcome this, we fabricate a vdW heterostructure capacitor with a metal-insulator-semiconductor-metal (MISM) architecture using 10-nm-thick multilayer hexagonal-BN (hBN) to suppress excess leakage. (Fig. 2d; see Supplementary Fig. 6 for device manufacture). Figure 2e shows *P*–*E* loops for the ST-3R MoS<sub>2</sub> capacitor, where  $E_{\text{MoS}_2}$  is the effective electric field across the ST-3R MoS<sub>2</sub> layer (Supplementary Note 3). For clarity, we present hysteresis loops at three selected values of electric fields, 0.027 V nm<sup>-1</sup>, 0.190 V nm<sup>-1</sup> and 0.217 V nm<sup>-1</sup>. The size of the hysteresis loop remains almost the same for  $E_{\text{MoS}_2}$  from 0.190 V nm<sup>-1</sup> to 0.217 V nm<sup>-1</sup>, indicating that the hysteresis becomes almost saturated. Supplementary Note 4 describes a systematic analysis of the experimental *P*–*E* hysteresis behaviour based on a modified Miller et al. model<sup>14,5</sup>. The analysis of the remnant polarization ( $P_r$ ) as a function of the maximum electric field ( $E_{\text{MoS}_2,\text{max}}$ ) shows that a step-like increase in  $P_r$  occurs at  $E_{\text{MoS}_2,\text{max}} = 0.109$  V nm<sup>-1</sup> (Fig. 2f).

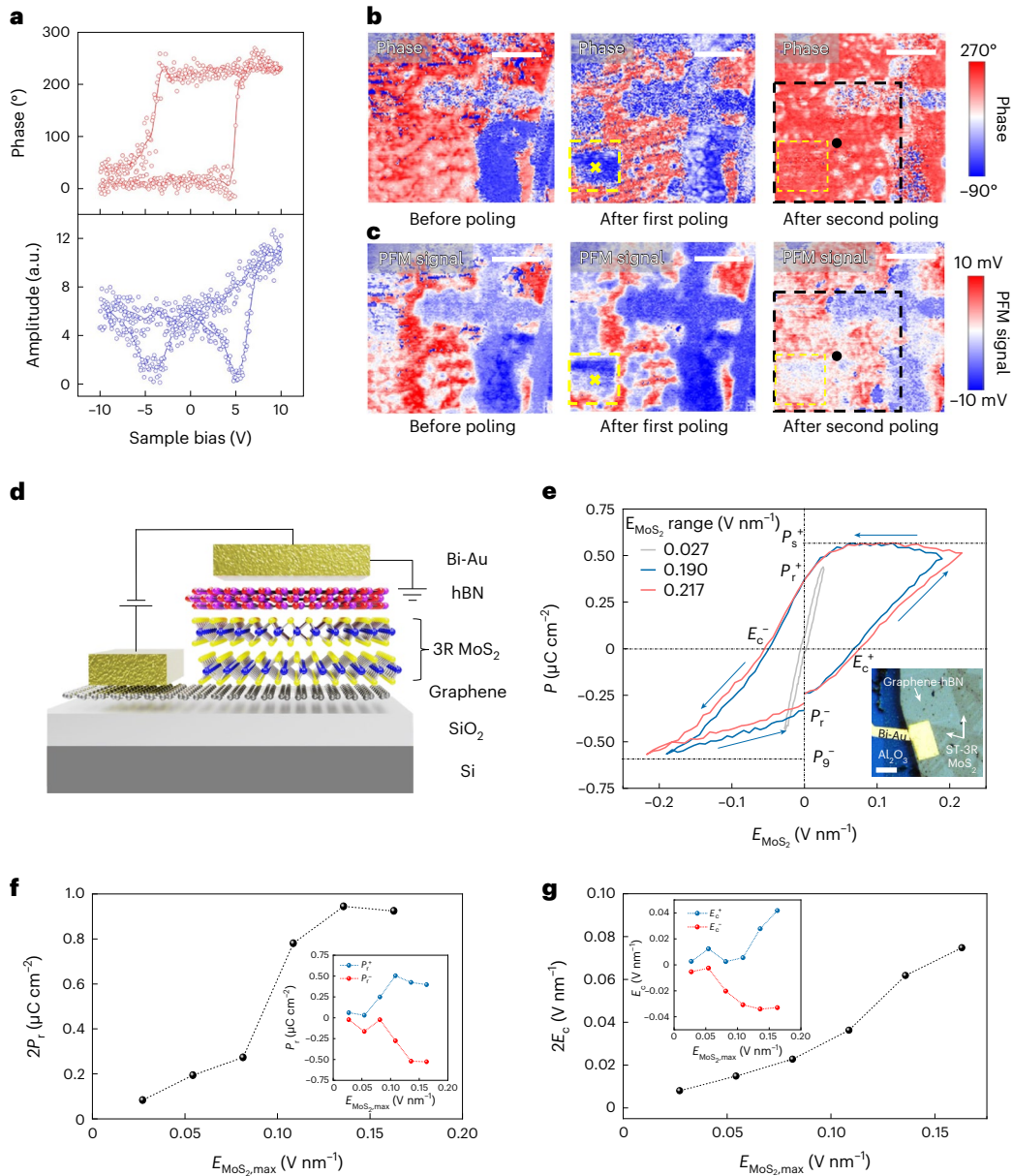


**Fig. 2 | PFM measurements, the vdW 3R MoS<sub>2</sub> capacitor and the ferroelectric property of the ST-3R bilayer MoS<sub>2</sub>.** **a**, Phase  $\theta$  and amplitude  $A$  of piezoresponse signal versus sample bias, showing the typical ferroelectric hysteresis and butterfly loop, respectively. **b**, **c**, PFM images (**b**), piezoresponse phase  $\theta$  and piezoresponse signal  $A \cos \theta$  (**c**) of ST-3R MoS<sub>2</sub> before and after multiple poling. In **b** and **c**, first, the yellow square was poled by  $-3.4$  V sample bias, and second, the black square was poled by  $+3.6$  V sample bias. In **b**, phases  $0^\circ$  and  $180^\circ$  correspond to downward and upward polarizations, respectively. Scale bars,  $400$  nm. **d**, Schematic of the Bi/hBN/3R MoS<sub>2</sub>/graphene capacitive

device on the SiO<sub>2</sub>/Si substrate. The hBN layer used here is about  $10$  nm thick and serves as an insulating layer to suppress leakage. **e**, Polarization-electric-field loops for the ST-3R MoS<sub>2</sub> capacitor.  $P$ ,  $E_{\text{MoS}_2}$ ,  $P_s$ ,  $P_r$  and  $E_c$ , denote the polarization, effective electric field across the MoS<sub>2</sub>, saturated polarization, remnant polarization and coercive field, respectively. Inset: optical micrograph of the measured ST-3R MoS<sub>2</sub> device. Scale bar,  $10$   $\mu$ m. **f**, **g**, Electric-field dependence of  $2P_r$  and  $2E_c$  obtained from the measured 3R MoS<sub>2</sub> capacitor in **e**, respectively. Insets, evolutions of the positive and negative  $P_r$  and  $E_c$  with the increasing range of applied electric field.

This suggests a minimum field applied across the MoS<sub>2</sub> bilayers that can trigger the movement of domain walls, where the coercive field ( $E_c$ ) is  $-0.036$   $V$   $nm^{-1}$  (Fig. 2g). The  $E_c$  strength is low compared with typical thin-film ferroelectrics<sup>25,26</sup> (about  $0.1$ – $1$   $V$   $nm^{-1}$ ) and twisted-3R WSe<sub>2</sub> bilayers<sup>17</sup> ( $0.3$   $V$   $nm^{-1}$ ). Density-functional-theory (DFT) calculations predict that the switching field for sliding ferroelectricity is low due to the sliding mechanism<sup>27,28</sup>. The observed  $E_c$  slightly deviates from the twisted-3R counterpart (Supplementary Table 1), which can be attributed to the distinct domain boundaries arrangement. In twisted-3R bilayers, the domain boundaries are shown in a moiré pattern, where dislocations annihilate at the immobile AA-stacking spots

serving as pinning sites to the domain boundaries. Thus, extra energy is needed to compensate for dislocation bending during domain switching. However, in the ST-3R MoS<sub>2</sub>, the partial dislocations are arranged in parallel without structural pinning points to constrain the movement of domain boundaries. This makes the measured coercive field lower, as theoretically predicted for interlayer sliding<sup>27,28</sup>. Meanwhile, from a technological standpoint, the overall coercive field produced in the MISM capacitor configuration is preferred to and differs from that of metal–ferroelectric–metal capacitors, due to distinct voltage distributions in each MISM layer. The correction relation about  $E_c$  is discussed in Supplementary Note 3. Another concern is the dielectric polarization

of the MoS<sub>2</sub> and hBN layers, since ferroelectric polarization in sliding ferroelectric systems is relatively weak compared with conventional ferroelectric systems. In fact, the effective dielectric polarization of MoS<sub>2</sub> and hBN is in the same order as ferroelectric polarization. Thus, its contribution cannot be ignored in the *P–E*-loops analysis. The competing process between ferroelectric and dielectric polarization deserves to be noted (Supplementary Note 4 and Extended Data Fig. 6). Once the dielectric leakage takes place in the high electric-field regime, the effect of dielectric polarization becomes nearly negligible in the *P–E*-loops analysis.

Note that similar capacitive loops as that in Fig. 2e might arise from the charge-trapping effect or be found in lossy dielectrics (that is, bananas ferroelectrics<sup>29</sup>). For comparison, control capacitor devices made of monolayer MoS<sub>2</sub> indicate that all the capacitor devices were operated in the Fowler–Nordheim (F–N) tunnelling regime<sup>30,31</sup> during *P–E* measurements, wherein hBN serves as tunnelling layers (Supplementary Fig. 7). Despite the leakage associated with the F–N tunnelling, the *P–E* curves measured from the control devices exhibit a normal dielectric capacitive behaviour with a negligible level of leakage. This implies that neither charge trapping nor tunnelling is dominant enough to account for the observed hysteresis in ST-3R vdW capacitors. To further exclude the contributions from charge trapping and the tunnelling-induced current, positive-up negative-down (PUND) measurement is conducted to obtain ferroelectric switching responses from 3R MoS<sub>2</sub> (Supplementary Fig. 8). The extracted *P–E* loop shows a *P<sub>r</sub>* of about 0.4 μC cm<sup>-2</sup>, consistent with that shown in Fig. 2f. A similar *P<sub>r</sub>* implies that dielectric leakage was not dominant enough to cause overestimation of the *P<sub>r</sub>* in the *P–E*-loops analysis. Based on these examinations, we confidently infer that the *P–E* hysteresis loops obtained from ST-3R MoS<sub>2</sub> capacitors are mainly attributable to ferroelectric switching.

## Sliding ferroelectric semiconductor transistor

Combined functionality of data processing and storage is being pursued for computing-in-memory devices<sup>32</sup>. For that context, we evaluate the performances of an ST-3R MoS<sub>2</sub> memory-transistor (Methods), which features a back-gated structure with 30-nm-thick SiO<sub>2</sub> and 10-nm-thick hBN layers to form the double-layer dielectric and ST-3R MoS<sub>2</sub> as the ferroelectric semiconductor channel (Fig. 3a; Supplementary Fig. 9 for device manufacture). The hBN dielectric is used to prevent the effect of oxide-related traps<sup>33,34</sup> that would interfere with the measured device characteristics. All the electrical measurements were performed in ambient conditions unless otherwise noted. Figure 3b shows the transfer characteristics of a representative ST-3R MoS<sub>2</sub> FET, where the drain current (*I<sub>DS</sub>*) is acquired by sweeping the back gate voltage (*V<sub>GS</sub>*) from negative to positive values and then back to negative values at a fixed drain voltage (*V<sub>DS</sub>*) = −1 V. An on/off current ratio of 6 orders of magnitude is achieved. The relative shift of the threshold voltage (*V<sub>th</sub>*) in the opposite sweeps produces a counterclockwise hysteresis loop in the *I<sub>DS</sub>–V<sub>GS</sub>* curves. No noticeable hysteretic behaviour is observed when the *V<sub>GS</sub>* sweeping range is ≤ 2 V. This suggests that the ferroelectric polarization in the ST-3R MoS<sub>2</sub> channel could not be switched at this condition. Counterclockwise hysteresis loops appear when the *V<sub>GS</sub>* range is ≥ 3 V, indicating a minimum required *V<sub>GS</sub>* of 2–3 V for the onset of domain switching in the ST-3R MoS<sub>2</sub> channel. This minimum *V<sub>GS</sub>* (corresponding to electric fields of 0.05–0.075 V nm<sup>-1</sup>, defined by the hBN-SiO<sub>2</sub> gate stack) to obtain the memory window is close to the value of the applied electric field that can cause an appreciable *P–E* loop (Fig. 2f). With increasing *V<sub>GS</sub>* range, the hysteresis loop increases to obtain a larger memory window (*V<sub>MW</sub>*) with two non-volatile resistance states, denoted as the program and the erase states induced by the remnant downward and upward polarizations, respectively. The individual polarization states of the ST-3R MoS<sub>2</sub> channel are also reflected in the output (*I<sub>DS</sub>–V<sub>DS</sub>*) curves of the opposite *V<sub>GS</sub>* sweep directions (Supplementary Fig. 10). While the polarity switching in ST-3R MoS<sub>2</sub> FETs

leads to a noticeable counterclockwise hysteresis loop, control devices without domain boundaries on single 3R domains of CVD-grown 3R MoS<sub>2</sub> show a distinct, hysteresis-free phenomenon (Fig. 3c). Counterclockwise hysteresis was not observed for even larger *V<sub>GS</sub>* sweep ranges for all the fabricated single-domain-3R MoS<sub>2</sub> FETs (Supplementary Fig. 11a,b). Note that the *I<sub>DS</sub>–V<sub>GS</sub>* counterclockwise hysteresis is a necessary condition for ferroelectric switching but is not a sufficient condition. Given that other mechanisms, such as charge trapping<sup>33–35</sup> and ionic gating<sup>36,37</sup>, have also been reported to potentially lead to similar counterclockwise *I<sub>DS</sub>–V<sub>GS</sub>* hysteresis, a systematic analysis, combined with control experiments, is discussed in Supplementary Note 5 and Supplementary Figs. 12 and 13, to rule out the contributions from other origins rather than ferroelectric switching. For clarification, electrical characterizations performed in vacuum produce hysteresis loops that appear similar to those measured in ambient conditions (Extended Data Fig. 7a). In further temperature-dependent measurements (Extended Data Fig. 7b,c), hysteresis loops were observed to maintain below 100 K, and the memory *I<sub>on</sub>/I<sub>off</sub>* ratio changed by less than an order of magnitude with cooling from 298 K to 77 K. These examination results reveal that external adsorbates were not the main causes to the observed memory phenomena. Besides, with the metal–insulator–semiconductor capacitive architecture, we measured the *P–E* responses from the same devices used in the field-effect measurement. No ferroelectric switching signature was observed for the single-3R-domain MoS<sub>2</sub> FET (Supplementary Fig. 11c), which emphasizes the importance of domain boundaries for large-scale ferroelectric switching.

The spontaneous polarization of ST-3R MoS<sub>2</sub> channels should translate into an accumulation of polarization charges at the MoS<sub>2</sub>/hBN interface, enabling the redistribution of the accumulated charges during switching. To elucidate this, we analyse the dependence of the *V<sub>th</sub>* with increasing *V<sub>GS</sub>* range for both kinds of FETs (Fig. 3d). With the evident *V<sub>th</sub>* shift (~4.3 V) obtained from the ST-3R FET, the spontaneous polarization *P<sub>o</sub>* in the ST-3R MoS<sub>2</sub> channel is calculated to be 0.177 μC cm<sup>-2</sup> at its maximum (Supplementary Note 6). Given that, in principle, the *P<sub>s</sub>* is 0.56 μC cm<sup>-2</sup> for 3R MoS<sub>2</sub>, the memory window should be larger with the higher *V<sub>GS</sub>* (an estimated *P<sub>o</sub>* of ~0.297 μC cm<sup>-2</sup> is obtained at a *V<sub>GS</sub>* range of 10 V, see Supplementary Fig. 14). In contrast, the *V<sub>th</sub>* evolutions of the single-domain-3R MoS<sub>2</sub> FET are like those of the ST-3R FET in the forward sweep, indicating that the single-domain 3R MoS<sub>2</sub> channel possesses spontaneous, unswitchable upward polarization. On the other hand, the *I<sub>DS</sub>–V<sub>GS</sub>* hysteresis near *V<sub>GS</sub>* = 0 V in ST-3R MoS<sub>2</sub> FETs reveals a charge storage capability for non-volatile memory operation. Figure 3d also shows the *V<sub>MW</sub>* evolution of the ST-3R MoS<sub>2</sub> FET. The *V<sub>MW</sub>* becomes larger with increasing *V<sub>GS</sub>* range, meaning that more 3R domains are flipped in response to the gate field.

Other than the successful realization of the ferroelectric polarization switching in the ST-3R MoS<sub>2</sub> FET, device reliability must be evaluated for non-volatile memory applications. Figure 3e shows the retention characteristics of an ST-3R MoS<sub>2</sub> FET that was programmed and erased with a *V<sub>GS</sub>* of ±10 V for 1 s and was read via a floating gate and a *V<sub>DS</sub>* = −1 V, measured in an N<sub>2</sub> atmosphere. The non-volatile program and erase states, differing by four orders of magnitude, are measured within periods of up to 10<sup>4</sup> s. The projected retention reveals that individual states should be able to be maintained for a timescale of the order of years. This proves that long-term data retention at room temperature is feasible in the ST-3R MoS<sub>2</sub> FET, partially due to the high-quality vdW interfaces. The main reason is attributed to parallel-distributed, straight domain boundaries (Fig. 1d,g) in ST-3R MoS<sub>2</sub>. Thanks to the straight dislocation configuration, ST-induced domain boundaries are able to remain stationary for a time instead of returning, as with bending dislocations<sup>14,16,17</sup>, where the latter typically refer to anti-ferroelectricity. Consequently, the memory states of ST-3R MoS<sub>2</sub> FETs can be maintained even when the gate field is removed. However, retention loss due to charge trapping might still occur (Extended Data Fig. 8). Further improvement in encapsulation or passivation

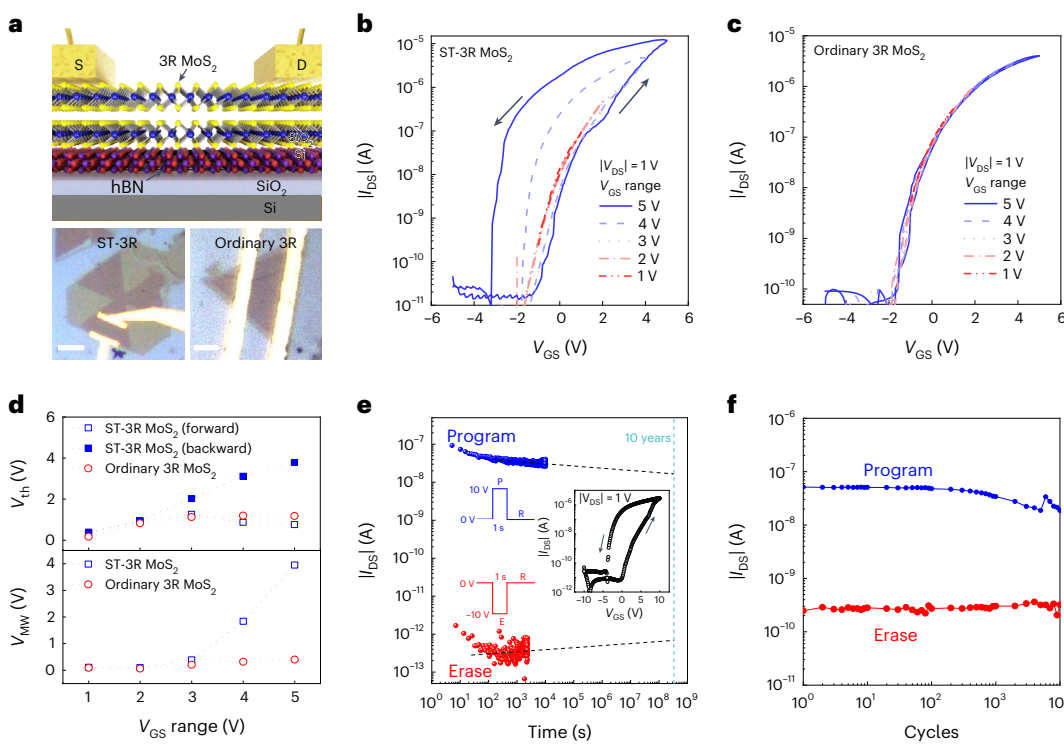


**Fig. 3 | Device characteristics of 3R MoS<sub>2</sub> sliding-ferroelectric FETs.**

**a**, Schematic of a proposed 3R MoS<sub>2</sub> ferroelectric transistor and the optical micrographs of the fabricated FETs with ST-3R and ordinary 3R MoS<sub>2</sub> as channels. The ordinary 3R MoS<sub>2</sub> sample refers to the case of a single 3R domain. Scale bars, 5  $\mu\text{m}$ . **b,c**, Transfer characteristics of an ST-3R MoS<sub>2</sub> FET (**b**) and ordinary 3R MoS<sub>2</sub> FET (**c**) at  $|V_D| = 1$  V at increasing  $V_{GS}$  sweep ranges, from  $\pm 1$  V to  $\pm 5$  V, showing a stark comparison between hysteretic (**b**) and hysteresis-free (**c**) behaviour.

**d**, Top,  $V_{GS}$  range dependence of the threshold voltage and bottom, the memory

window of the ST-3R (**b**) and ordinary 3R (**c**) FETs. **e**, Retention of the program and erase currents of an ST-3R MoS<sub>2</sub> FET with floating gate at  $|V_{DS}| = 1$  V on a 10<sup>4</sup>-second period, measured in an N<sub>2</sub> atmosphere. Gate pulses of 10 V and -10 V at 1 s were used for the program and erase operations, respectively. The  $I_{DS}$ - $V_{GS}$  curves are shown in the inset for reference. **f**, Endurance of the program and erase currents of an ST-3R MoS<sub>2</sub> FET at  $|V_D| = 1$  V and  $V_{GS} = -3.9$  V after 10<sup>4</sup> cycles of the alternating 1- $\mu\text{s}$  gate pulses of +10 V and -10 V.

techniques is necessary. Figure 3f shows the endurance characteristics of the device that was switched up to 10<sup>4</sup> cycles between the program and erase states using 1  $\mu\text{s}$  poling pulses. The two individual resistance states having two orders of magnitude differences are stable and rewritable without significant degradation. This indicates that the movement of domain boundaries and the associated domain evolution is reversible without the dragging effect caused by structural defects or the device edge. High-speed operation is achieved with microsecond program and erase times that are limited by the global back-gated structure. Theoretical works have predicted that 2D displacive transformations via van der Waals sliding are an extremely fast process within a sub-nanosecond timescale<sup>38,39</sup>; thus, an ultrahigh-speed operation with program and erase times much shorter than those used here can be expected.

A successive  $I_{DS}$ - $V_{GS}$  measurement on the same device repeated for 50 cycles exhibits a repeatable memory window and stable dual-sweep  $V_{th}$  positions (Extended Data Fig. 9a). A statistical analysis of 50 devices fabricated on the same SiO<sub>2</sub>/Si chip exhibits a normal distribution of  $V_{MW}$  and memory  $I_{on}/I_{off}$  ratio (Extended Data Fig. 9b,c). The repeatability and stability are attributed to the clean vdW interface that ensures undisturbed dipole switching via the interlayer shear motion. Device parameters and performances of 2D FeS-FETs and Fe-FETs in recent studies are surveyed in Table 1 and Supplementary Table 3. The Fe-S-FET technology is still in its infancy, and its device physics deserves to be explored for future memory applications. However, 2D ferroelectric semiconductors have been explored and are still limited compared to the large party of ferroelectric insulators<sup>40,41</sup>. Of many 2D semiconductors studied, MoS<sub>2</sub> possesses a high carrier mobility and has

been validated experimentally using high-current devices, making it a promising channel material for future low-power electronics<sup>42</sup>. Besides, MoS<sub>2</sub> is expected to be the most industry-relevant 2D semiconductor material based on the recent progress in large-scale monocrystalline MoS<sub>2</sub> growth<sup>19,20,43</sup>. Since ferroelectricity is restored in the 3R MoS<sub>2</sub> channel of the FET, gate materials selection is another degree of freedom for transistor operation. Using a 10 nm hBN and 30 nm SiO<sub>2</sub> gate stack, the average memory window of about 7 V is obtained for ST-3R MoS<sub>2</sub> FETs via a write voltage of 10 V. With continuous scaling of gate oxides down to the advanced technology nodes, sliding ferroelectric transistors might potentially be concerned about the memory window shrinkage because of small coercive fields that are determined by the vdW sliding mechanism. Considering that the write voltage is required to meet an on-chip, logic-compatible level (<1.2 V) in advanced complementary metal-oxide semiconductor (CMOS) devices for low-power applications<sup>1</sup>, low switching voltage ferroelectric is pursued<sup>6,7,10</sup>. Accordingly, the memory window needs not to be as large as the presented case. Combined with ultra-scaled gate oxides, the inherent small coercive field of bilayer 3R MoS<sub>2</sub> could still enable a memory window with low supply voltages, which is desirable for low-power non-volatile memory and logic devices.

## Conclusions

We have reported ferroelectric semiconductor transistors that are based on polarity switching in 3R MoS<sub>2</sub> epilayers. The observed shear transformation overcomes the challenge of creating mobile domain boundaries in the growth of ordinary 3R MoS<sub>2</sub>. The presence of Shockley partial based domain boundaries is crucial in achieving switchable

**Table 1 | Device parameters and performance metrics of ST-3R MoS<sub>2</sub> FETs and 2D FeS-FETs in the literatures**

Ref.	Ferroelectric	Channel	$t_{FE}$ (nm)	Maximum $I_{on}/I_{off}$	Memory window (V)	Retention (s)	Endurance (cycles)	Write voltage (V) and field (V nm <sup>-1</sup> ) <sup>a</sup>	Write speed <sup>b</sup> (s)
2	$\alpha\text{-In}_2\text{Se}_3$	$\alpha\text{-In}_2\text{Se}_3$	79	$10^8$	~3	N/A	N/A	N/A	N/A
47	$\alpha\text{-In}_2\text{Se}_3$	$\alpha\text{-In}_2\text{Se}_3$	20–50	$>10^5$	12.5	>150	250	$\pm 6, \pm 0.12$	<0.2
48	$\alpha\text{-In}_2\text{Se}_3$	$\alpha\text{-In}_2\text{Se}_3$	52	$>10^3$	4	N/A	N/A	N/A	N/A
48	$\alpha\text{-In}_2\text{Se}_3/\text{CIPS}$	$\alpha\text{-In}_2\text{Se}_3$	52	$10^6$	14.47	>10 <sup>4</sup>	>10 <sup>4</sup>	$\pm 5, \pm 0.056$	1
49	$\alpha\text{-In}_2\text{Se}_3$	$\alpha\text{-In}_2\text{Se}_3$	40	$>10^4$	6	>500	>500	$\pm 8, \pm 0.16$	$4 \times 10^{-8}$
50	SnS <sup>b</sup>	SnS	3.7	>10	N/A <sup>c</sup>	>10 <sup>3</sup>	>10 <sup>4</sup>	$\pm 7, \pm 0.0014^d$	<2 × 10 <sup>-2</sup>
16	Twisted-3R MoS <sub>2</sub>	Twisted-3R MoS <sub>2</sub>	~1.3	~1.37	N/A <sup>c</sup>	~3 × 10 <sup>3</sup>	>10	$\pm 10, \pm 0.58$	120
This work	ST-3R MoS <sub>2</sub>	ST-3R MoS <sub>2</sub>	1.3	>10 <sup>6</sup>	7	>10 <sup>4</sup>	>10 <sup>4</sup>	<10, <10.25	<10 <sup>-6</sup>

$t_{FE}$ , ferroelectric thickness. <sup>a</sup>The write voltage and speed are extracted mainly from endurance tests and sometimes from retention tests. The write field is calculated from the write voltage divided by the gate dielectric thickness. <sup>b</sup>In-plane ferroelectric field-effect transistor. <sup>c</sup>Logarithmic  $I_{DS}-V_{GS}$  plots are not available. <sup>d</sup>The write field is calculated from the bias voltage divided by the channel length.

electric polarization. While previous studies of sliding ferroelectricity have explored domain switching based on moiré ferroelectricity, our ST-3R MoS<sub>2</sub> demonstrates the generalization of the switching concept for epitaxial films. Using bilayer ST-3R MoS<sub>2</sub> as an ultrathin-body FeS-FET channel (1.3 nm) also should lead to less engineering and manufacturing complexity than an approach using twisted TMD or WSe<sub>2</sub> bilayers<sup>16</sup>.

Our system fits the requirement of sub-3 nm nodes in upcoming CMOS technologies, in which atomic-scale channel thickness is needed to minimize short channel effects and achieve low OFF-state leakage current, ensuring good gate control for very-large-scale integration and data storage applications. Our work highlights the potential of 2D sliding ferroelectric channels for continued memory-transistor scaling down to the 5 nm or even sub-3 nm technology nodes. Together with recent breakthroughs in MoS<sub>2</sub> transistors—including ultralow contact resistance via semi metallic bismuth<sup>44</sup>, p-type behaviour via high-work-function contact metals<sup>45</sup> and integration with ultrahigh-k dielectrics<sup>46</sup>—we expect that our ST-mediated sliding ferroelectricity could provide a path to all-MoS<sub>2</sub>-based electronics with logic and memory functionalities.

## Methods

### CVD synthesis

The homoepitaxial growth of ST-3R MoS<sub>2</sub> was achieved using an ambient-pressure CVD system. Before synthesis, 90 nm SiO<sub>2</sub>/Si substrates used for growth were ultrasonically cleaned sequentially in acetone for 10 min, isopropanol for 5 min, deionized water for 10 min and finally dried with nitrogen gas. High-quality S (99.99% purity) and MoO<sub>3</sub> (99.9% purity) powders, purchased from Sigma-Aldrich, were used as the precursor sources. The reaction furnace was a quartz tube (4 inches in diameter) with three heating coils. A schematic drawing of the CVD setup is portrayed in Extended Data Fig. 1a. A crucible containing 10 mg MoO<sub>3</sub> was placed at the centre of the furnace tube. An SiO<sub>2</sub> substrate was put on another crucible placed 0.5 cm behind the MoO<sub>3</sub> boat, for growth. A crucible containing 350 mg S powder was located upstream in excess. High purity Ar ( $\geq 99.99\%$ ), used as a carrier gas, was passed at a flow rate of 424 standard cubic centimetres per minute during the entire growth process. A two-step reaction temperature profile was used (Extended Data Fig. 1b); the furnace was first ramped up with a rate of  $25.7\text{ }^\circ\text{C min}^{-1}$  to 800 °C and held at 800 °C for 3 min and was then cooled down to 670 °C within 5 min and stabilized for 17 min. The S zone started to heat 2 min before the MoO<sub>3</sub> zone reached 800 °C and was kept within 200–250 °C as the MoO<sub>3</sub> zone underwent the tempering process at 670 °C. The furnace underwent natural furnace cooling to room temperature. Extended Data Fig. 1 shows the key CVD parameters to grow ST-3R MoS<sub>2</sub> flakes.

### Wet transfer process

Poly(methyl methacrylate) (PMMA) was used as the supporting film to peel off MoS<sub>2</sub> flakes from the SiO<sub>2</sub> substrate. PMMA was spin-coated on the top of MoS<sub>2</sub> samples at 4000 r.p.m. for 90 s, followed by baking at 110 °C for 3 min. The edge of the PMMA film was scribed by a blade and was immersed slowly into an 80 °C 0.03 M KOH solution. The PMMA film carrying MoS<sub>2</sub> samples could easily be peeled off after soaking it in the KOH solution for less than 30 min. Before fishing it up onto the destination substrate, the floating PMMA/MoS<sub>2</sub> film was subsequently rinsed with deionized water many times. After baking at 110 °C for 1 h, the PMMA film was finally removed with acetone. The PMMA-assisted wet transfer method was also utilized for transferring graphene and hBN, where a 0.01 M (NH<sub>4</sub>)<sub>2</sub>S<sub>2</sub>O<sub>8</sub> solution was used as the etchant. A continuous hBN film (10 nm thick) and a continuous graphene film were purchased from CL Technology Co., Ltd. The process flow for fabricated FET and capacitive devices is provided in Supplementary Figs. 6 and 9.

### Optical and topographic characterizations

The optical properties of MoS<sub>2</sub> films were characterized using Raman and photoluminescence (PL) spectroscopic measurements. The Raman and PL spectra were taken using an integrated confocal optical microscope system with a spectrometer (Kymera 328i, Andor) and a 532 nm (2.33 eV) continuous-wave laser as the excitation source. A  $\times 100$  objective lens with a numerical aperture of 0.9, and a variable 150 lines mm<sup>-1</sup> and 1,200 lines mm<sup>-1</sup> grating were employed to obtain a better signal-to-noise ratio. For topographic measurements, a Nanoview 1000 AFM system was employed, operating in the tapping mode, by using the tip model Olympus OMCL-AC160TS (tip stiffness, 26 N m<sup>-1</sup>; frequency, 300 kHz). All the measurements were conducted under ambient conditions.

### STM characterization

ST-3R MoS<sub>2</sub> bilayer flakes were transferred onto a highly oriented pyrolytic graphite (HOPG) substrate. Before measurement, the MoS<sub>2</sub>/HOPG substrate was subjected to vacuum annealing at 200 °C for 12 h in a UHV chamber to remove surface impurities. Scanning tunnelling microscope spectroscopy (Omicron RT STM) was conducted in a UHV chamber with vacuum and temperature conditions kept at  $5 \times 10^{-10}$  Torr and room temperature, respectively. Band structures were studied by STS. The tungsten STM tip used for measurement was manufactured by the sodium hydroxide chemical etching method.

### TEM investigations

To prepare TEM specimens, ST-3R MoS<sub>2</sub> films were transferred onto a TEM grid (Quantifoil Mo grid). TEM observations were conducted using dark-field for stacking analysis and scanning TEM (STEM) modes

for atomic structure analysis. All the observations were performed on an aberration corrected JEM-ARM200FTH with a cold-field emission gun and a spherical-aberration corrector (the JEOL DELTA-corrector), operating at 80 kV. Parts of selected-area diffraction pattern (SADP) were captured in an FEI Tecnai G2 F20 operating at 200 kV. All the experiments were performed at room temperature.

### XPS characterization

X-ray photoelectron spectroscopy ( $\mu$ -XPS) measurement was performed using the scanning photoemission spectroscopy (SPESM) at the 09A1 beamline of National Synchrotron Radiation Research Center (NSRRC) in Taiwan. ST-3R MoS<sub>2</sub> flakes were transferred to an Au-coated SiO<sub>2</sub>/Si substrate. Before measurement, the samples were prebaked at 180 °C in vacuum at  $10^{-9}$  Torr for 12 h, and XPS measurement was performed at room temperature. The photon source was a U5-SGM undulator with photon energy set to 400 eV. The incident X-ray beam size was  $0.1\text{ }\mu\text{m}$ . The passing energy was set to 0.75 eV.

### PFM measurement

PFM measurements were conducted using a commercial scanning probe microscope system (Multimode 8, Bruker). The PFM hysteresis loops were measured using an on-off field switching spectroscopic technique. During the on-field stage, the ferroelectric polarization was switched by external bias, while the piezoresponse signals were acquired in the off-field remanent state to minimize the electrostatic effects. To measure the hysteresis, a Pt/Ir-coated tip with a spring constant of  $2.8\text{ N m}^{-1}$  (NANOSENSORS PPP-EFM) was employed. The tip was driven with an rms AC voltage of 1 V, operating at a contact-resonance frequency of approximately 300 kHz. For scanning PFM images, a soft Pt/Ir-coated tip with a spring constant of  $0.2\text{ N m}^{-1}$  (NANOSENSORS PPP-CONTPT) was utilized, and the applied AC voltage of 1 V was driven at the contact-resonance frequency of approximately 200 kHz.

### Polarization measurement

Bi/hBN/MoS<sub>2</sub>/graphene capacitive MIS devices of ST-3R MoS<sub>2</sub> and monolayer MoS<sub>2</sub> were fabricated via the same manufacturing process, for which step-by-step details are portrayed in Supplementary Fig. 6. In brief, wet transfer, e-beam lithography and Ar plasma etching were repeatedly performed to fabricate the bottom three layers from graphene to hBN, followed by making top Bi/Au electrodes via e-beam lithography and thermal evaporation. Ferroelectric properties and switching experiments were carried out using a commercial ferroelectric tester (Radiant Technologies, Inc.). The ferroelectric polarization–electric-field loops were measured at 1 kHz square voltage input. PUND measurements were carried out using the Keysight B1530 with a waveform generator fast measurement unit installed in Keysight B1500A semiconductor analyser. The voltage waveforms for the PUND measurements are six triangle pulses with a delay of 10  $\mu\text{s}$  and amplitude of 2 V. The first three pulses are for the preset, positive switching pulse and up unswitched pulse. The last three pulses are for preset, negative switching pulse and unswitched down pulse. All the measurements were performed in ambient conditions.

### Field-effect measurement

The PMMA-assisted wet transfer method was used to fabricate a continuous 10-nm-thick hBN film onto a prepatterned 30 nm SiO<sub>2</sub>/Si substrate, followed by the wet transfer of ST-3R MoS<sub>2</sub> samples onto the hBN-covered substrate. Mask for etching and electrode deposition was made by spin-coating with PMMA photoresist at 4000 r.p.m. for 55 s, followed by baking at 180 °C for 3 min. Source and drain electrodes were patterned by performing e-beam lithography in a scanning electron microscope (JEOL JSM-6500F), and the substrate was then developed in an IPA/MIBK solution. All the unnecessary areas of hBN and MoS<sub>2</sub> were etched away by the Ar plasma treatment. Contact metals consisting of 20 nm Bi and 40 nm Au were deposited by a custom-built

thermal evaporator (JunSun Tech Co. Ltd.) at a rate of  $1\text{ \AA s}^{-1}$ . Acetone was used to do a final liftoff to obtain back-gated MoS<sub>2</sub> FETs. After the liftoff, the device substrate was baked at 120 °C for 3 min. A Keithley 2636B source metre was used to acquire the current–voltage characteristics. Detailed process flow of ST-3R MoS<sub>2</sub> FETs and control devices is portrayed in Supplementary Fig. 9. All the measurements were performed in ambient conditions unless otherwise noted.

### Computational methods

Our calculations are performed using DFT implemented in the Vienna Ab initio Simulation Package (see details in refs. 27,28). The generalized gradient approximation with the Perdew–Burke–Ernzerhof exchange-correlation functional and the projector augmented wave potentials are adopted. The kinetic energy cut-off is 400 eV, and a large vacuum space is set in the vertical direction, so the nearest distance between two neighbouring bilayers is greater than  $15\text{ \AA}$ . For geometric optimization, the Brillouin zone is sampled with  $12 \times 12 \times 1\text{ k}$  points using the Monkhorst–Pack scheme, while the forces on all atoms are optimized to be less than  $0.005\text{ eV/\AA}$  and the tolerance for the energy convergence is set to  $10^{-5}\text{ eV}$ . Grimme's Perdew–Burke–Ernzerhof D2 functional is used to account for dispersive forces, the Berry phase method is employed to evaluate crystalline polarization, and the ferroelectric switching pathway is computed by using nudged elastic band method.

### Data availability

Source data are provided with this paper. All other data that support the findings in this study are available from the corresponding authors upon reasonable request.

### References

1. Khan, A. I., Keshavarzi, A. & Datta, S. The future of ferroelectric field-effect transistor technology. *Nat. Electron.* **3**, 588–597 (2020).
2. Mikolajick, T., Slesazeck, S., Park, M. H. & Schroeder, U. Ferroelectric hafnium oxide for ferroelectric random-access memories and ferroelectric field-effect transistors. *MRS Bull.* **43**, 340–346 (2018).
3. Si, M. et al. A ferroelectric semiconductor field-effect transistor. *Nat. Electron.* **2**, 580–586 (2019).
4. Miller, S., Nasby, R., Schwank, J., Rodgers, M. & Dressendorfer, P. Device modeling of ferroelectric capacitors. *J. Appl. Phys.* **68**, 6463–6471 (1990).
5. Ni, K., Jerry, M., Smith, J. A. & Datta, S. A circuit compatible accurate compact model for ferroelectric-FETs. In *IEEE Symposium on VLSI Technology*, 131–132 (IEEE, 2018); <https://doi.org/10.1109/VLSIT.2018.8510622>
6. Jiang, Y. et al. Enabling ultra-low-voltage switching in BaTiO<sub>3</sub>. *Nat. Mater.* **21**, 779–785 (2022).
7. Cheema, S. S. et al. Enhanced ferroelectricity in ultrathin films grown directly on silicon. *Nature* **580**, 478–482 (2020).
8. Ahn, C. H., Rabe, K. M. & Triscone, J. M. Ferroelectricity at the nanoscale: local polarization in oxide thin films and heterostructures. *Science* **303**, 488–491 (2004).
9. Mehta, R. R., Silverman, B. D. & Jacobs, J. T. Depolarization fields in thin ferroelectric films. *J. Appl. Phys.* **44**, 3379–3385 (1973).
10. Cheema, S. S. et al. Emergent ferroelectricity in subnanometer binary oxide films on silicon. *Science* **376**, 648–652 (2022).
11. Tan, A. J. et al. Ferroelectric HfO<sub>2</sub> memory transistors with high-k interfacial layer and write endurance exceeding  $10^{10}$  cycles. *IEEE Electron Dev. Lett.* **42**, 994–997 (2021).
12. Hoffmann, M. et al. Fast read-after-write and depolarization fields in high endurance n-type ferroelectric FETs. *IEEE Electron Dev. Lett.* **43**, 717–720 (2022).

13. Yasuda, K., Wang, X., Watanabe, K., Taniguchi, T. & Jarillo-Herrero, P. Stacking-engineered ferroelectricity in bilayer boron nitride. *Science* **372**, 1458–1462 (2021).
14. Vizner Stern, M. et al. Interfacial ferroelectricity by van der Waals sliding. *Science* **372**, 1462–1466 (2021).
15. Rogée, L. et al. Ferroelectricity in untwisted heterobilayers of transition metal dichalcogenides. *Science* **376**, 973–978 (2022).
16. Weston, A. et al. Interfacial ferroelectricity in marginally twisted 2D semiconductors. *Nat. Nanotechnol.* **17**, 390–395 (2022).
17. Wang, X. et al. Interfacial ferroelectricity in rhombohedral-stacked bilayer transition metal dichalcogenides. *Nat. Nanotechnol.* **17**, 367–371 (2022).
18. Miao, L. P. et al. Direct observation of geometric and sliding ferroelectricity in an amphidynamic crystal. *Nat. Mater.* **21**, 1158–1164 (2022).
19. Wang, Q. et al. Layer-by-layer epitaxy of multi-layer MoS<sub>2</sub> wafers. *Natl Sci. Rev.* **9**, nwac077 (2022).
20. Liu, L. et al. Uniform nucleation and epitaxy of bilayer molybdenum disulfide on sapphire. *Nature* **605**, 69–75 (2022).
21. Kim, J. H. et al. Interface-driven partial dislocation formation in 2D heterostructures. *Adv. Mater.* **31**, e1807486 (2019).
22. Zhang, Z. & Lagally, M. G. Atomistic processes in the early stages of thin-film growth. *Science* **276**, 377–383 (1997).
23. Witten, T. A. & Sander, L. M. Diffusion-limited aggregation. *Phys. Rev. B* **27**, 5686–5697 (1983).
24. Weston, A. et al. Atomic reconstruction in twisted bilayers of transition metal dichalcogenides. *Nat. Nanotechnol.* **15**, 592–597 (2020).
25. Park, J. Y. et al. A perspective on semiconductor devices based on fluorite-structured ferroelectrics from the materials–device integration perspective. *J. Appl. Phys.* **128**, 240904 (2020).
26. Peng, Y. et al. Nanocrystal-embedded-insulator (NEI) ferroelectric FETs for negative capacitance device and non-volatile memory applications. *Nanoscale Res. Lett.* **14**, 115 (2019).
27. Wu, M. & Li, J. Sliding ferroelectricity in 2D van der Waals materials: related physics and future opportunities. *Proc. Natl Acad. Sci. USA* **118**, e2115703118 (2021).
28. Li, L. & Wu, M. Binary compound bilayer and multilayer with vertical polarizations: two-dimensional ferroelectrics, multiferroics, and nanogenerators. *ACS Nano* **11**, 6382–6388 (2017).
29. Scott, J. F. Ferroelectrics go bananas. *J. Phys.: Condens. Matter* **20**, 021001 (2008).
30. Sarker, B. K. & Khondaker, S. I. Thermionic emission and tunneling at carbon nanotube–organic semiconductor interface. *ACS Nano* **6**, 4993–4999 (2012).
31. Beebe, J. M., Kim, B., Gadzuk, J. W., Frisbie, C. D. & Kushmerick, J. G. Transition from direct tunneling to field emission in metal-molecule-metal junctions. *Phys. Rev. Lett.* **97**, 026801 (2006).
32. Wu, M. Two-dimensional van der Waals Ferroelectrics: scientific and technological opportunities. *ACS Nano* **15**, 9229–9237 (2021).
33. Jeon, H. et al. Hysteresis modulation on Van der Waals-based ferroelectric field-effect transistor by interfacial passivation technique and its application in optic neural networks. *Small* **16**, e2004371 (2020).
34. Kaushik, N. et al. Reversible hysteresis inversion in MoS<sub>2</sub> field effect transistors. *npj 2D Mater. Appl.* <https://doi.org/10.1038/s41699-017-0038-y> (2017).
35. Park, Y., Baac, H. W., Heo, J. & Yoo, G. Thermally activated trap charges responsible for hysteresis in multilayer MoS<sub>2</sub> field-effect transistors. *Appl. Phys. Lett.* <https://doi.org/10.1063/1.4942406> (2016).
36. Wang, H., Wu, Y., Cong, C., Shang, J. & Yu, T. Hysteresis of electronic transport in graphene transistors. *ACS Nano* **4**, 7221–7228 (2010).
37. Wang, B. et al. Monolayer MoS<sub>2</sub> synaptic transistors for high-temperature neuromorphic applications. *Nano Lett.* **21**, 10400–10408 (2021).
38. Xu, H., Zhou, J., Li, Y., Jaramillo, R. & Li, J. Optomechanical control of stacking patterns of h-BN bilayer. *Nano Res.* **12**, 2634–2639 (2019).
39. Park, J., Yeo, I. W., Han, G., Hwang, C. S. & Choi, J. H. Ferroelectric switching in bilayer 3R MoS<sub>2</sub> via interlayer shear mode driven by nonlinear phononics. *Sci. Rep.* **9**, 14919 (2019).
40. Guan, Z. et al. Recent progress in two-dimensional ferroelectric materials. *Adv. Electron. Mater.* **6**, 1900818 (2019).
41. Qi, L., Ruan, S. & Zeng, Y. J. Review on recent developments in 2D ferroelectrics: theories and applications. *Adv. Mater.* **33**, e2005098 (2021).
42. Liu, Y. et al. Promises and prospects of two-dimensional transistors. *Nature* **591**, 43–53 (2021).
43. Li, T. et al. Epitaxial growth of wafer-scale molybdenum disulfide semiconductor single crystals on sapphire. *Nat. Nanotechnol.* **16**, 1201–1207 (2021).
44. Shen, P. C. et al. Ultralow contact resistance between semimetal and monolayer semiconductors. *Nature* **593**, 211–217 (2021).
45. Wang, Y. et al. P-type electrical contacts for 2D transition-metal dichalcogenides. *Nature* **610**, 61–66 (2022).
46. Huang, J. K. et al. High-k perovskite membranes as insulators for two-dimensional transistors. *Nature* **605**, 262–267 (2022).
47. Wang, L. et al. Exploring ferroelectric switching in α-In<sub>2</sub>Se<sub>3</sub> for neuromorphic computing. *Adv. Funct. Mater.* **30**, 2004609 (2020).
48. Baek, S. et al. Ferroelectric field-effect-transistor integrated with ferroelectrics heterostructure. *Adv. Sci.* **9**, e2200566 (2022).
49. Wang, S. et al. Two-dimensional ferroelectric channel transistors integrating ultra-fast memory and neural computing. *Nat. Commun.* **12**, 53 (2021).
50. Kwon, K. C. et al. In-plane ferroelectric tin monosulfide and its application in a ferroelectric analog synaptic device. *ACS Nano* **14**, 7628–7638 (2020).

## Acknowledgements

This work was supported by the National Science and Technology Council (NSTC) of Taiwan through grant 111-2124-M-003-005 (Y.-W.L.), 111-2119-M-008-003-MBK (Y.-W.L.), 110-2634-F-009-027 (C.-L.L.), 110-2112-M-A49-013-MY3 (C.-L.L.) and 110-2112-M-A49-022-MY2 (C.-L.L.). Y.-W.L. thanks the Taiwan Consortium of Emergent Crystalline Materials (TCECM) for its financial support. C.-L.L. thanks the Center for Semiconductor Technology Research (CSTR) for its financial support (the CSTR is from The Featured Areas Research Center Program within the framework of the Higher Education Sprout Project by the Ministry of Education (MOE) in Taiwan). T.H.Y. thanks C. R. Kao at Materials Science and Engineering, National Taiwan University, for his insightful comments on dislocation analyses and the phase transformation model. We thank Y.-M. Chang in The Instrumentation Center at National Tsing Hua University for her skilled TEM operation. We are grateful for technical support on SPEM data acquisition from Y.-C. Kuo, S.-H. Hsieh and C.-H. Chen at National Synchrotron Radiation Research Center (NSRRC) and K.-H. O. Yang at National Taiwan University.

## Author contributions

T.H.Y. and B.-W.L. contributed equally to this work. T.H.Y. and Y.-W.L. conceived the idea and devised the project. H.-C.H. and Yi-Cheng Chen conducted the material growth. L.Y. and M.W. performed the DFT simulation to deduce the sliding mechanism. T.H.Y., H.-C.H., W.-H.C., H.-C.L. and Y.-C. Chang prepared samples for material characterizations. F.-X.C. and Y.-H.K. performed the scanning tunnelling microscope spectroscopy analysis and the cycling

*I-V* measurement. S.-Z.H. and Yi-Chun Chen conducted PFM investigations and analysed the data. P.-Y.L. conducted the HRTEM and SADP investigation. T.H.Y. did the dislocation analysis and verified the formation and sliding mechanisms of domain boundaries. T.H.Y., H.-C.L. and W.-H.C. designed and fabricated MISIM capacitors and FETs. T.H.Y., B.-W.L. and T.-H.K. performed the field-effect measurements. Y.-J.H. supported the FET fabrication and data analysis. T.H.Y., B.-W.L., T.-H.K. and J.-H.C. conducted the *P-E* measurements, and K.-S.L. examined the validity and interpretation of the results. T.H.Y. and B.-W.L. performed the PUND measurements, and Z.-F.L. and M.-H.L. assisted with the data analysis and interpretation. T.H.Y. and Y.-S.K. did the Wulff net simulation. T.H.Y., H.-C.H., Y.-F.C. and T.-H.L. performed the Raman and PL analyses. T.H.Y. and H.-C.H. conducted the SPEM investigation. H.-C.H. and A.C.C. conducted the AFM analyses. The manuscript was written by T.H.Y., B.-W.L., H.-C.H., K.B.S. and F.-X.C. with detailed discussion with all authors and was revised by C.-L.L., M.W. and Y.-W.L. The overall project was supervised by Y.-W.L.

## Competing interests

The authors declare no competing interests.

## Additional information

**Extended data** is available for this paper at  
<https://doi.org/10.1038/s41928-023-01073-0>.

**Supplementary information** The online version contains supplementary material available at  
<https://doi.org/10.1038/s41928-023-01073-0>.

**Correspondence and requests for materials** should be addressed to Tilo H. Yang, Chun-Liang Lin or Yann-Wen Lan.

**Peer review information** *Nature Electronics* thanks the anonymous reviewers for their contribution to the peer review of this work.

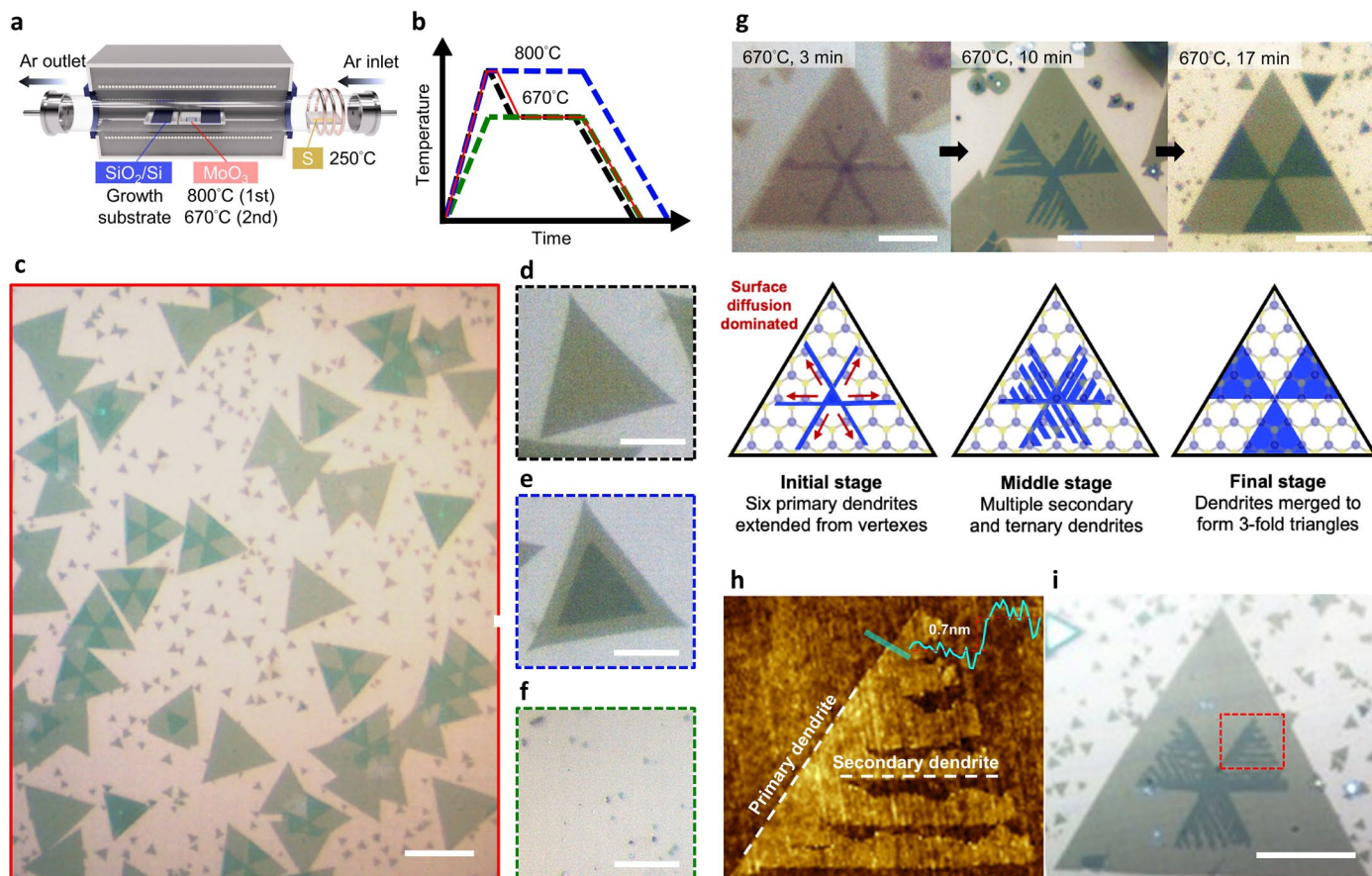
**Reprints and permissions information** is available at  
[www.nature.com/reprints](http://www.nature.com/reprints).

**Publisher's note** Springer Nature remains neutral with regard to jurisdictional claims in published maps and institutional affiliations.

Springer Nature or its licensor (e.g. a society or other partner) holds exclusive rights to this article under a publishing agreement with the author(s) or other rightsholder(s); author self-archiving of the accepted manuscript version of this article is solely governed by the terms of such publishing agreement and applicable law.

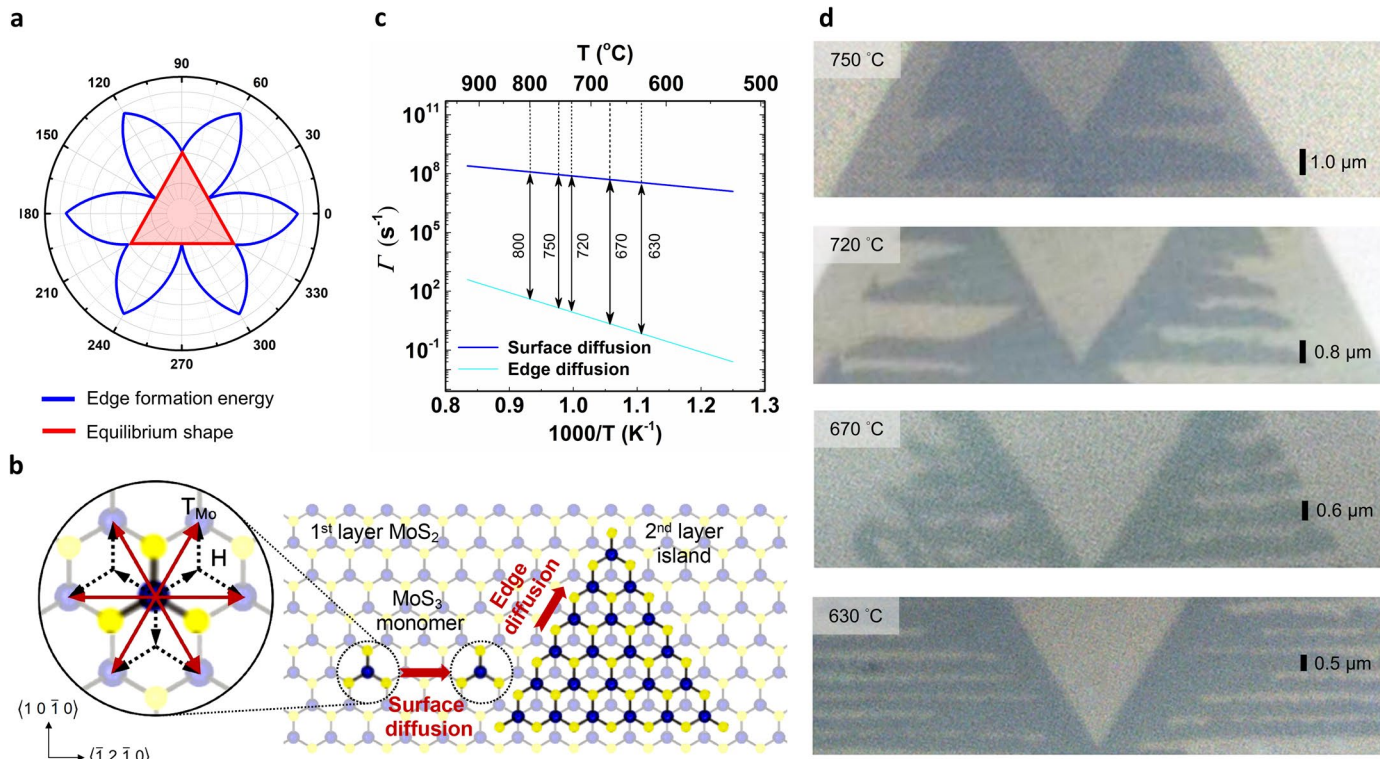
© The Author(s), under exclusive licence to Springer Nature Limited 2023

<sup>1</sup>Department of Physics, National Taiwan Normal University, Taipei, Taiwan. <sup>2</sup>Taiwan Semiconductor Research Institute, National Applied Research Laboratories, Hsinchu, Taiwan. <sup>3</sup>Department of Electrophysics, National Yang Ming Chiao Tung University, Hsinchu, Taiwan. <sup>4</sup>Department of Physics, National Cheng Kung University, Tainan, Taiwan. <sup>5</sup>School of Physics, Huazhong University of Science and Technology, Wuhan, P. R. China. <sup>6</sup>Institute of Cellular and Organismic Biology, Academia Sinica, Taipei, Taiwan. <sup>7</sup>Department of Mathematics and Physics, University of Santo Tomas, Manila, Philippines. <sup>8</sup>Program for Semiconductor Devices, Materials, and Hetero-integration, Graduate School of Advanced Technology, National Taiwan University, Taipei, Taiwan. <sup>9</sup>Center for Measurement Standards, Industrial Technology Research Institute (ITRI), Hsinchu, Taiwan. <sup>10</sup>Department of Physics, National Taiwan University, Taipei, Taiwan. <sup>11</sup>Present address: Department of Electrical Engineering and Computer Science, Massachusetts Institute of Technology, Cambridge, MA, USA.  e-mail: [thy@mit.edu](mailto:thy@mit.edu); [clin@nycu.edu.tw](mailto:clin@nycu.edu.tw); [ywlanc@ntnu.edu.tw](mailto:ywlanc@ntnu.edu.tw)

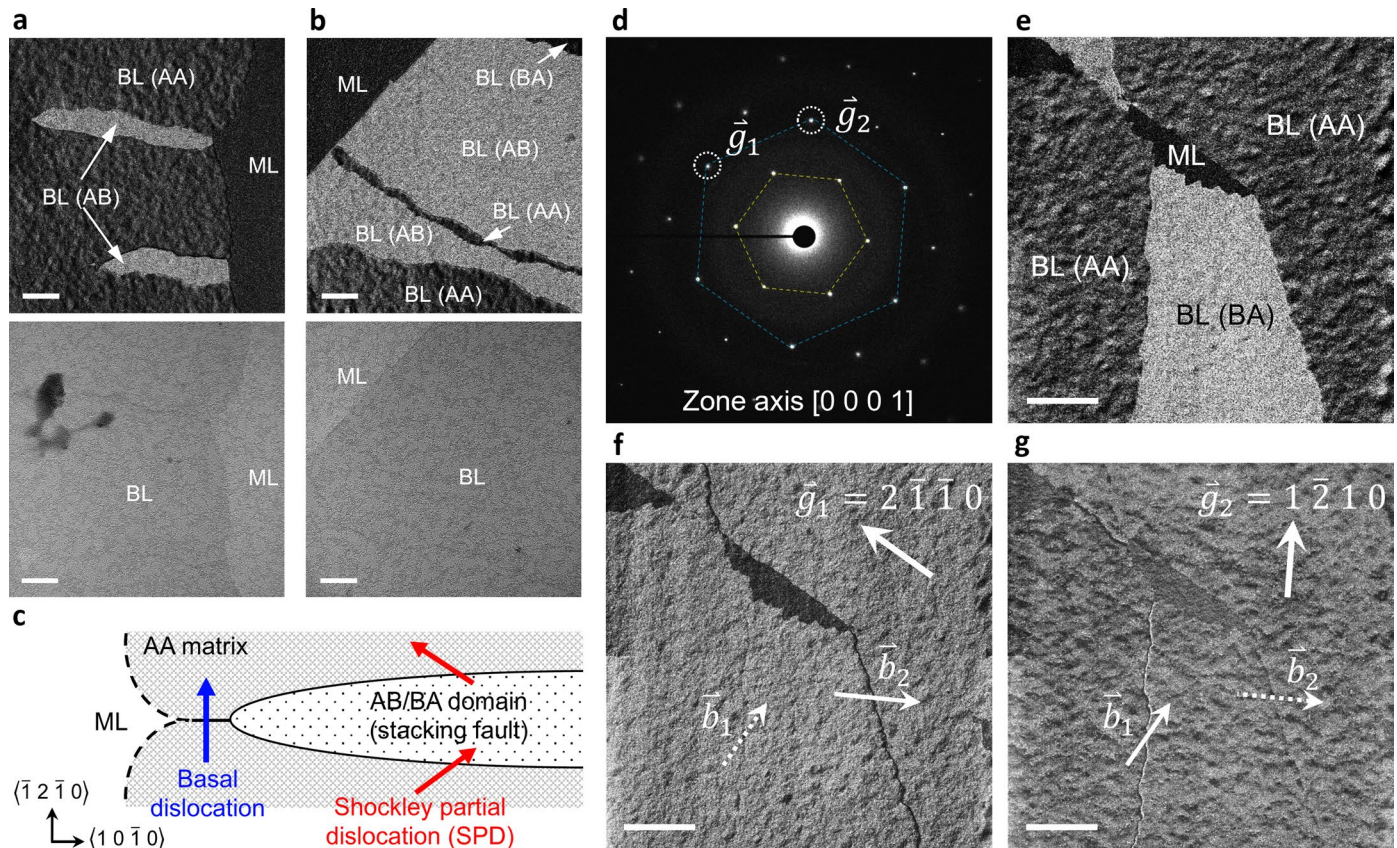

**Extended Data Fig. 1 | Controllable synthesis of ST-3R MoS<sub>2</sub> epilayers.**

**a**, CVD setup for ST-3R MoS<sub>2</sub> synthesis. A two-step CVD synthesis was performed at 800 °C for 3 min and 670 °C for 17 min, respectively. The higher temperature selected for the first step was to intensively vaporize MoO<sub>3</sub>, which was subsequently brought to the growth substrate by an Ar carrier gas. An additional SiO<sub>2</sub>/Si substrate was placed in front of the MoO<sub>3</sub> powders for gas flow modulation. **b**, Clarification of the growth conditions for ST-3R MoS<sub>2</sub> epilayers by changing temperatures and duration times of the MoO<sub>3</sub> zone. The MoS<sub>2</sub> flakes produced with different thermal histories, denoted in different color lines, are shown in (c-f). **c**, ST-3R bilayer MoS<sub>2</sub> flakes *via* a two-step synthesis: 800 °C for 3 min (1<sup>st</sup> step) and 670 °C for 17 min (2<sup>nd</sup> step). Scale bar, 20 μm. **d**, Monolayer MoS<sub>2</sub> *via* a two-step synthesis: 800 °C for 2 min (1<sup>st</sup> step) and 670 °C for 17 min (2<sup>nd</sup> step). The Mo amount in this condition is insufficient to promote vertical growth. **e**, Concentric growth of 3R MoS<sub>2</sub> epilayers *via* a one-step synthesis at 800 °C for 20 min, showing 3R MoS<sub>2</sub> flakes commonly observed in CVD synthesis. **f**, Nucleation of MoS<sub>2</sub> does not take place *via* a one-step synthesis at 670 °C for 20 min. Scale bars in (d-f), 10 μm. The results of (c-f) suggest that the first duration mainly determined the Mo supply for MoS<sub>2</sub> growth at 800 °C. However, the growth under the continuous Mo supply at 800 °C led to ordinary concentric-bilayer MoS<sub>2</sub>. A confined Mo amount and relatively low temperature is a key condition for the ST-3R bilayer MoS<sub>2</sub> growth.

**g**, Optical micrographs showing morphological evolutions of ST-3R MoS<sub>2</sub> bilayers grown on SiO<sub>2</sub>/Si substrates with the increasing duration time at 670 °C. The bottom panel illustrates the corresponding growth stages. The epilayer growth can be divided into three stages: (1) formation of six primary dendrites with the preferred orientations along the armchair directions, (2) formation of multiple secondary and tertiary dendrites based on the primary dendrites, and (3) coalescence of parallelly-oriented dendrites to form a merged epilayer triangle. Scale bars, 20 μm. **h**, AFM topography image of the marked bilayer region in the optical micrograph (g) of an ST-3R MoS<sub>2</sub> flake, showing a monolayer step height of about 0.7 nm for the epitaxial nanoribbons. Scale bar, 10 μm.

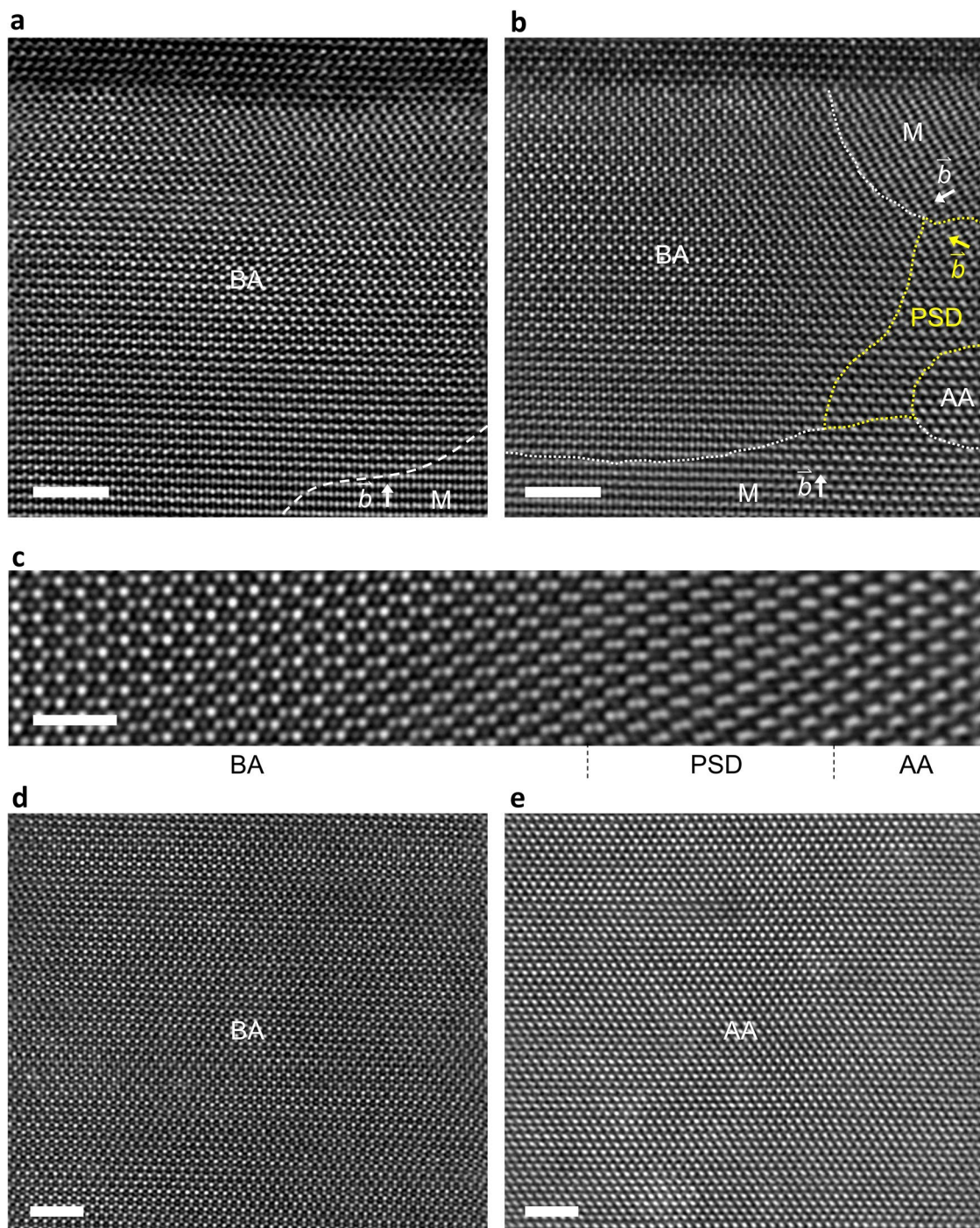


**Extended Data Fig. 2 | Growth mechanism of ST-3R MoS<sub>2</sub> homoepitaxy.** **a**, Polar plots of the formation energies of MoS<sub>2</sub> edges as a function of chiral angle  $\chi$  ( $0^\circ \leq \chi \leq 360^\circ$ ) under a Mo-deficient environment. The interior red triangle represents the final equilibrium shape of a MoS<sub>2</sub> epilayer. The  $0^\circ$  corresponds to the armchair direction. **b**, Schematic of surface and edge diffusion for a MoS<sub>3</sub> monomer on 1H-MoS<sub>2</sub> surface. The stacking configuration between the 2<sup>nd</sup> layer and the underlying MoS<sub>2</sub> layer is 3R stacking. The enlarged illustration shows possible migration pathways of a MoS<sub>3</sub> monomer adsorbed on top of the Mo site, where the black dashed arrows denote the hopping paths for every single hopping event while the red solid arrows are the effective paths of two consecutive hopping events which possess the equivalent vectors parallel to the  $\langle 1\bar{2}\bar{1}0 \rangle$  (armchair) directions. T<sub>Mo</sub>, the top site of Mo atoms from the 1<sup>st</sup> layer. H, the hollow site. **c**, Arrhenius relation of the hopping rates of a MoS<sub>3</sub> monomer for the surface and edge diffusion. **d**, Tuning dimensionality of bilayer nanoribbons by changing the 2<sup>nd</sup> (tempering) temperature, as denoted by black dashed lines in (c), clearly showing that the bilayer ribbons became thinner with decreasing the temperature. The observed behavior is reasonable since the decrease in growth temperature increased the difference in the diffusion rates between surface diffusion and edge diffusion. The more limited the ability of edge relaxation is, the higher the degree of fractal growth and the thinner the bilayer ribbons turn out.



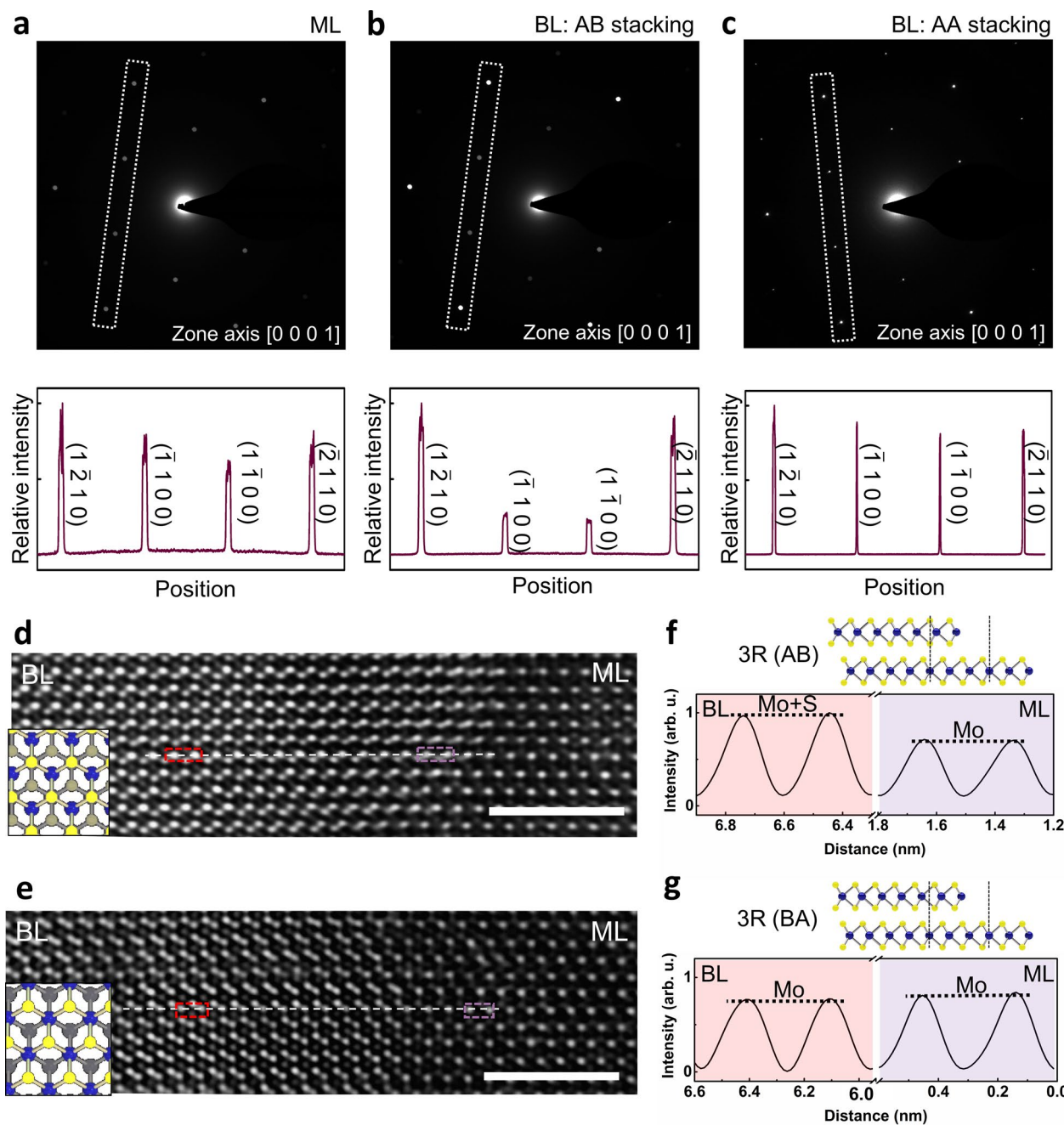
**Extended Data Fig. 3 | Shear-transformation-induced 3R polytypic domains and domain boundaries.** **a, b**, Extended dark-field (top) and bright-field (bottom) TEM images taken with the  $(10\bar{1}0)$  diffraction spot, revealing AB and BA lamellae in the AA matrix. All the lamellar domains show the preferred orientation along the zigzag directions, which is roughly perpendicular to the growth direction of bilayer nanoribbons. Scale bars, 100 nm. **c**, Schematic of AB and BA stacking faults forming in the unstable AA matrix, where the domain boundaries constitute a pair of Shockley partial dislocations (SPD) with  $b \parallel \langle 10\bar{1}0 \rangle$  that is decomposed from a basal dislocation  $b \parallel \langle \bar{1}2\bar{1}0 \rangle$ . ML refers to monolayer, while BL to bilayer. **d**, A diffraction pattern from the ST-3R bilayer

nanoribbon shown in (e). **e**, Tilted dark-field TEM image obtained by filtering the  $(10\bar{1}0)$  diffraction spot of MoS<sub>2</sub>, where a BA lamella is embedded in an AA matrix. **f**, **g**, Dark-field TEM images from the same region in (e), taken with  $\vec{g}_1 = (2\bar{1}\bar{1}0)$  and  $\vec{g}_2 = (1\bar{2}10)$  diffraction spots denoted in (d), respectively. Based on the criterion  $\vec{g} \cdot \vec{b} = 0$  that is satisfied to make dislocations disappear, the domain boundary  $b_1$  disappears with  $\vec{g}_1 = (2\bar{1}\bar{1}0)$  while the domain boundary  $b_2$  disappears with  $\vec{g}_2 = (1\bar{2}10)$ . This suggests that BA-AA domain boundaries constitute a pair of Shockley partial dislocations with  $b \parallel \langle 10\bar{1}0 \rangle$ , and the resultant BA domain is a Shockley stacking fault forming in the AA matrix. Scale bars, 20 nm.



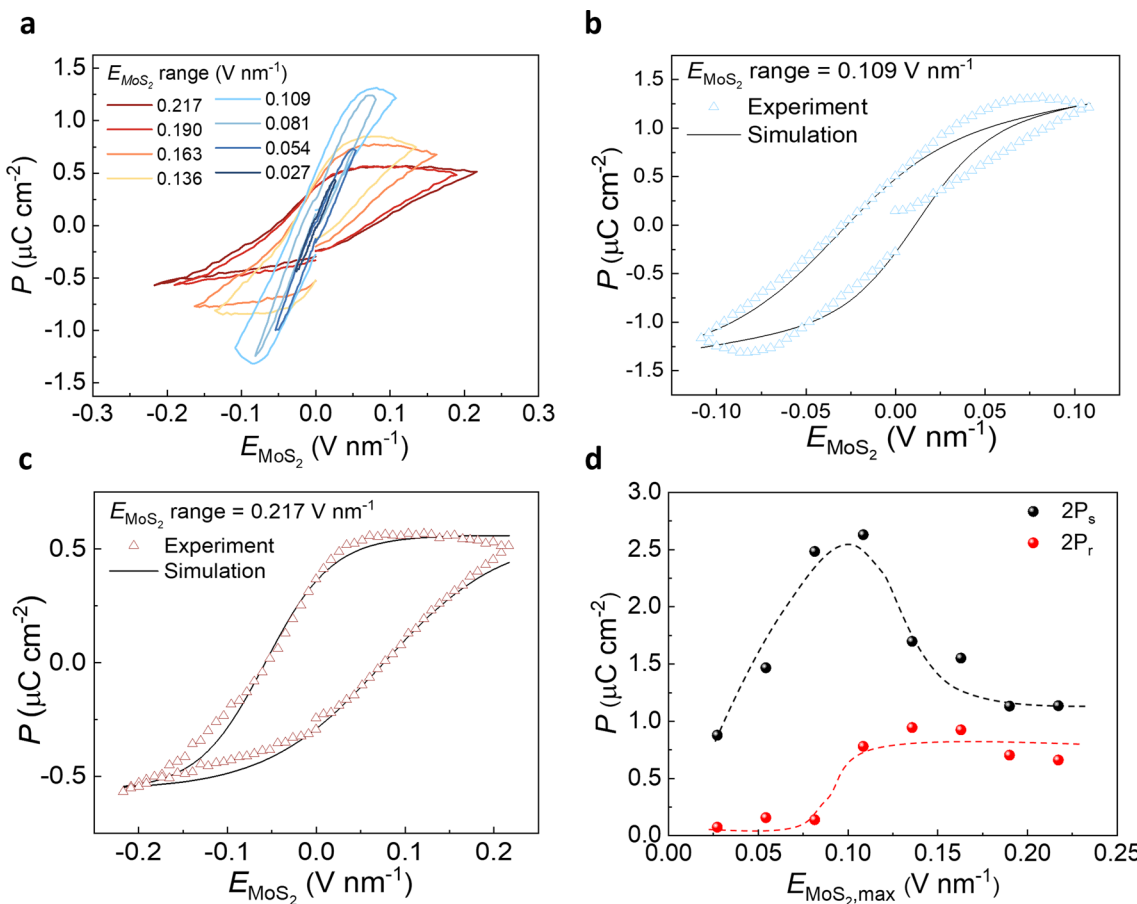
**Extended Data Fig. 4 | Extended STEM-ADF image analysis of shear-transformation-induced 3R domain boundaries.** **a, b**, STEM-ADF images taken from two neighboring regions in a 3R nanoribbon, showing a BA-AA domain boundary. (M: moiré-like transition zone. PSD: partial screw dislocation). The Burgers vectors of the M zone and the PSD site are parallel to the  $\langle 10\bar{1}0 \rangle$  direction.

Scale bars, 2 nm. **c**, Enlarged image showing the transition of atomic-stacking configuration between the AA and BA domains in (b). Scale bar, 1 nm. **d, e**, STEM-ADF images taken from the regions far from the domain boundary shown in (b). No noticeable lattice misalignment is found in the separated domains. Scale bars, 2 nm.



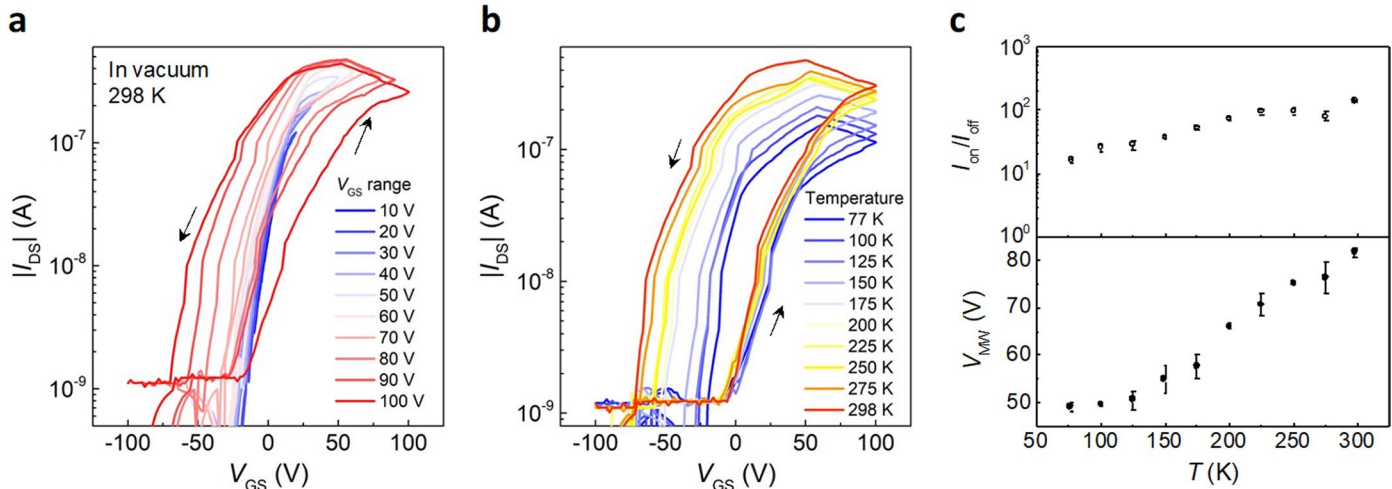
**Extended Data Fig. 5 | Diffraction patterns and STEM-ADF images of different 3R stacking domains.** **a–c**, SADPs taken from monolayer, AB-stacking bilayer, and AA-stacking bilayer regions, respectively. The corresponding intensity profiles were extracted along the white dashed square in each SADP image of

(a–c), which are consistent with simulated SADPs of 3R stacking polytypes by Kim et al. (Ref. 21). **d, e**, STEM-ADF images showing atomic arrangements of AB and BA domains, respectively. Scale bars, 2 nm. **f, g**, Intensity profiles extracted from the red and purple dashed squares in the bilayer and monolayer regions in (d,e).



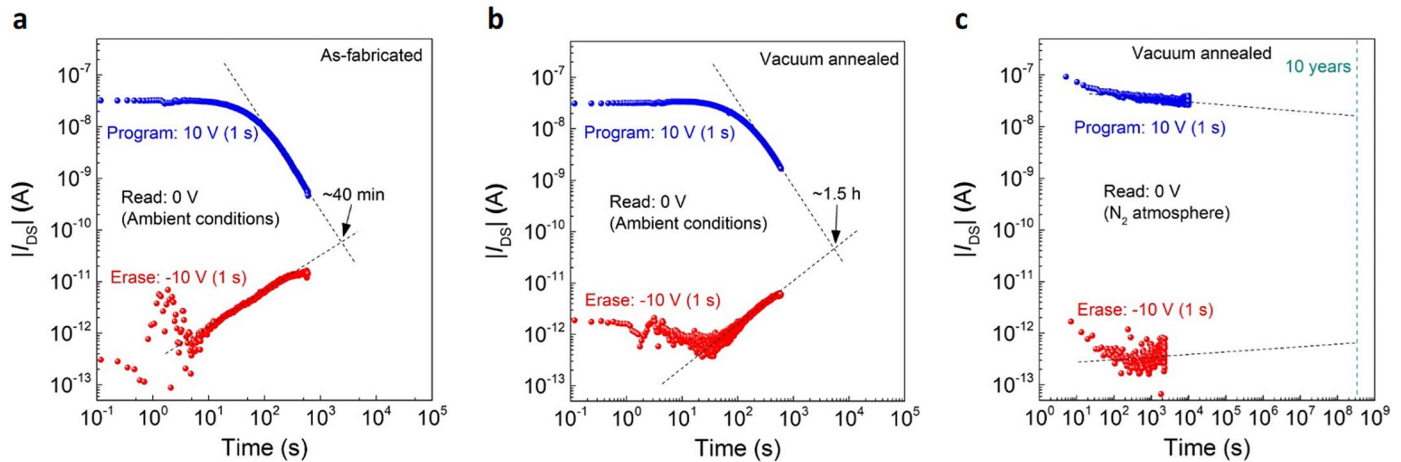
**Extended Data Fig. 6 | Evolution of experimental P-E loops of ST-3R MoS<sub>2</sub> capacitor and mathematical modeling.** **a**, P-E loops of the ST-3R MoS<sub>2</sub> capacitor at increasing  $E_{\text{MoS}_2}$  ranges, from 0.027 V nm<sup>-1</sup> to 0.217 V nm<sup>-1</sup>.  $E_{\text{MoS}_2}$  is the effective field across the ST-3R MoS<sub>2</sub> layer (Supplementary Note 3). **b**, The experimental and simulated P-E loops, from the corrected Miller et al. model, at  $E_{\text{MoS}_2} = 0.109$  V nm<sup>-1</sup>. To consider the asymmetric polarization switching due to

the different top and bottom interfacial structures of the ST-3R MoS<sub>2</sub> capacitor (top: hBN/MoS<sub>2</sub>, bottom: graphene/MoS<sub>2</sub>), the corrected Miller model is used to simulate the P-E loops<sup>4,5</sup>. **c**, The experimental data and corrected Miller model estimation of the P-E loops at  $E_{\text{MoS}_2} = 0.217$  V nm<sup>-1</sup>. **d**, Electric-field dependence of  $2P_s$  and  $2P_r$ , extracted from **a**.



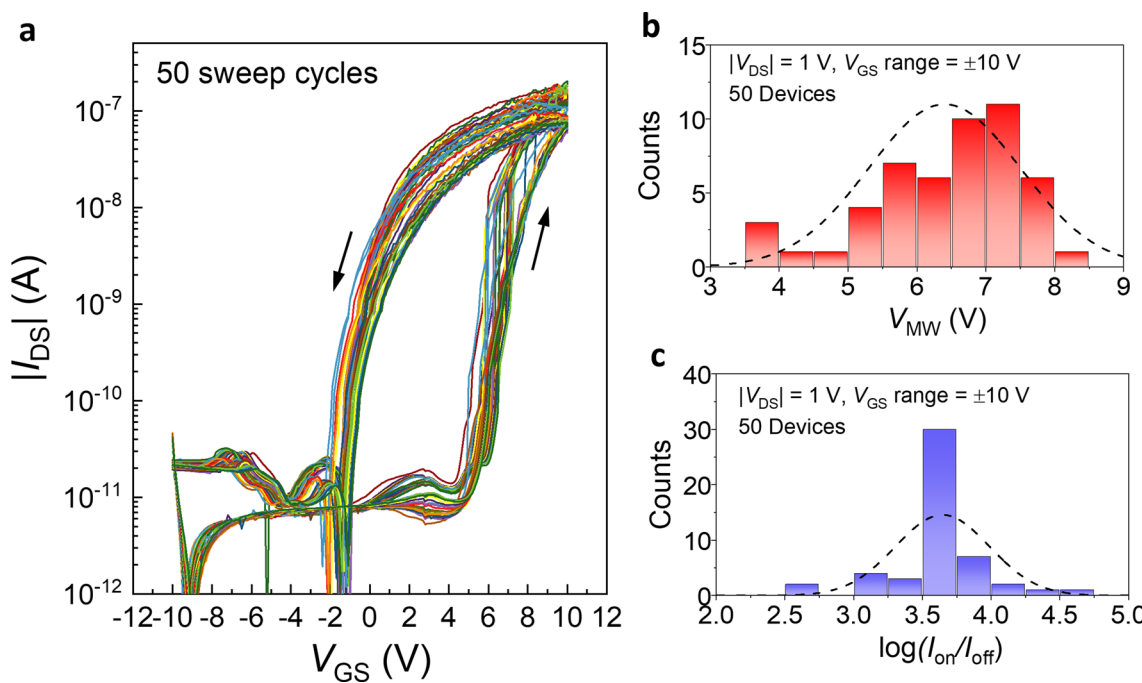
**Extended Data Fig. 7 | Temperature-dependent electrical measurements of ST-3R MoS<sub>2</sub> FETs.** The SiO<sub>2</sub> dielectric thickness for the FETs presented is 300 nm. The applied  $E$  fields (defined by applied voltages/the SiO<sub>2</sub> thickness) range from 0.033–0.33 V nm<sup>-1</sup>, which is quantitatively close to that used for the FETs with the 30 nm-thick SiO<sub>2</sub> dielectric. **a**, Transfer characteristics at  $|V_{DS}|=1$  V

at increasing  $V_{GS}$  sweep ranges, from  $\pm 10$  V to  $\pm 100$  V, measured in vacuum and at 298 K. **b**, Temperature-dependent transfer characteristics at  $|V_{DS}|=1$  V at  $V_{GS}$  range of  $\pm 100$  V. **c**, The temperature-dependent changes of the  $I_{on}/I_{off}$  ratio and the memory window ( $V_{MW}$ ).



**Extended Data Fig. 8 | Concerns of long-term retention arising from charge trapping.** Retention of the program and erase currents of an ST-3R MoS<sub>2</sub> FET with floating gate at  $|V_{DS}|=1$  V, for **a**, an as-fabricated device measured in ambient conditions, **b**, a vacuum-annealed device measured in ambient conditions, and

**c**, a vacuum-annealed device measured in an  $N_2$  atmosphere, respectively. The annealing was conducted at 100 °C for 30 min. Gate pulses of 10 V and -10 V at 1 s were used for the program and erase operations, respectively.



**Extended Data Fig. 9 | Statistical analysis on memory performance of ST-3R MoS<sub>2</sub> FETs.** **a**, The dual-sweep  $I_{DS}$ - $V_{GS}$  transfer curves repeated for 50 cycles from an ST-3R MoS<sub>2</sub> FET device. Cumulative distribution of **(b)**  $V_{MW}$  and **(c)** the on/off ratio of 50 ST-3R MoS<sub>2</sub> FET devices. The bias conditions,  $|V_{DS}|=1$  V and  $V_{GS}$  range =  $\pm 10$  V, are used to ensure that the FETs reach a maximum  $V_{MW}$  and a

maximum  $I_{on}/I_{off}$  ratio between the program and erase states. The distribution in each graph is fitted with a normal curve. The statistical distribution shows that  $V_{MW}$  is around 7 V, and the highest value can reach around 8–9 V. The on-off current ratio between the program and erase states is about  $10^4$  and with an average of  $6.10 \times 10^3$ .